MSc thesis in Geomatics for the Built Environment

# Detection of subsurface meltwater in East Antarctica using SAR Interferometry

Weiran Li

2018

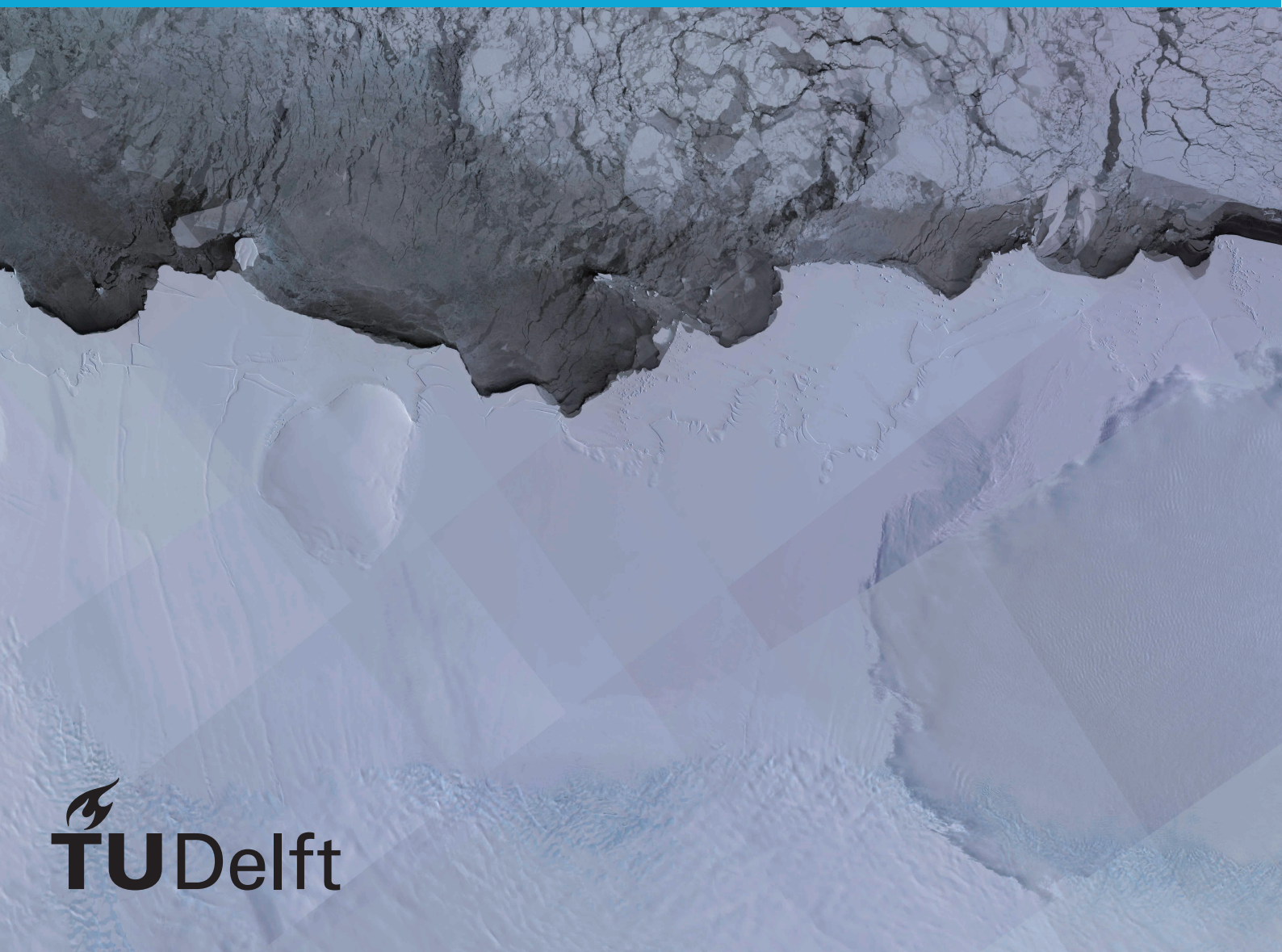

TU Delft

## ON COVER

An RGB image over Roi Baudouin Ice Shelf taken by Landsat 8 between 25/09/2017 and 05/10/2017. Generated with Google Earth Engine.

# DETECTION OF SUBSURFACE MELTWATER IN EAST ANTARCTICA USING SAR INTERFEROMETRY

A thesis submitted to the Delft University of Technology in partial fulfillment of the requirements for the degree of

**Master of Science**
in Geomatics for the Built Environment

by

Weiran Li

June 2018

The work in this thesis was made in the:

Department of Geoscience & Remote Sensing
Faculty of Civil Engineering & Geosciences
Delft University of Technology

and supported by:

Department of the OTB
Faculty of Architecture & the Built Environment
Delft University of Technology

| | |
|---|---|
| Supervisors: | Agung Indrajit, MSc |
| | Dr. F.J. (Paco) López-Dekker |
| | Dr. S.L.M. (Stef) Lhermitte |
| Co-reader: | Dr. Liangliang Nan |

# ABSTRACT

Climate change has been a heated topic in recent years, and the mass loss of ice sheets is one aspect of it. The Antarctic Ice Sheet has experienced certain mass loss in the form of ice-shelf collapse and (sub-)surface melting, but thorough study remains limited due to the remote location of the continent. Therefore, remote sensing is expected to provide valuable information on Antarctica, in order to monitor its mass balance and gain insights on the extent of climate change.

As one of the factors to the mass loss in Antarctica, subsurface melt can be critical yet hard to capture. The limitation of remote sensing data, especially valid optical images over polar regions may add to the issue. This study aims to exploit the potentiality of SAR Interferometry in detecting subsurface melt, as the microwave bands are not affected by weather and illumination, and the interferometric data may provide supportive information reflecting the properties of the physical environment. It is expected that by using this technique, the gap can be filled in when optical images are not available, or pure SAR images are not informative. The technique is applied to two ice shelves in East Antarctica, Roi Baudouin Ice Shelf and Amery Ice Shelf. And this study is expected to be operated over a broader scale such as the Antarctic continent and Greenland.

# ACKNOWLEDGEMENTS

First of all, I would like to thank Tjeu Lemmens, Hugo Ledoux and Agung Indrajit for giving me the opportunity to finish my graduation project in Faculty of Civil Engineering & Geosciences (CEG), and Dr Sandra Verhagen and Dr Miren Vizcaino for introducing me to my awesome supervisors, Paco López-Dekker and Stef Lhermitte, in the Department of Geoscience & Remote Sensing (GRS).

My sincere gratitude goes to Paco and Stef, for offering me this extremely interesting topic, for the invaluable expertise, and for the patience and enthusiasm in communicating with me. I cannot be more impressed by their encouragement and friendliness. It has been a great fortune for me to work with them.

Lots of thanks to Gert Mulder, for helping me with technical issues and explaining me supplementary knowledge. Ramon Hanssen, Freek van Leijen, and Floris Heuff also provided me with all kinds of support and interesting ideas. Martijn Meijers has also given helpful opinions within his field of expertise.

Thanks to Marc Rodriguez-Cassola and Pau Prats-Iraola, who went out of their way to introduce and explain some alternative algorithms to me. And special thanks go to Roderik Lindenbergh and Nan Liangliang, who would like to read the thesis and provide valuable opinions.

It has been nice to work in the lab provided by the Department of GRS, because of the relaxing atmosphere, and especially because of both the interesting technical and non-technical conversations with my collegues Jeroen van Heyningen, Zhou Kaixuan, Elyta Widyaningrum, Dun Han and Zhang Hao.

I would like to express my gratitude to my parents, my uncle and my friends who support me, especially to Wang Xiaowen, He Yuting, Luo Jie, Shi Danni, Liu Xiaoxu and Liu Yuzhang for dealing with my random chats and emotions.

Finally, thanks to Antarctica, just for being there.

# CONTENTS

# LIST OF FIGURES

# LIST OF TABLES

# LIST OF ALGORITHMS

# ACRONYMS

**AIS** Antartica Ice Sheet . . . 1
**ALOS** Advanced Land Observing Satellite . . . 18
**ASAR** Advanced SAR . . . 12
**CCC** coherent cross-correlation . . . xv
**CRS** coordinate reference system . . . 58
**DEM** digital elevation model . . . xi
**DJF** December, January, February . . . 18
**DORIS** Delft Object-oriented Radar Interferometric Software . . . 10
**EPSG:3031** Antarctic Polar Stereographic . . . 6
**ESD** enhanced spectral diversity . . . 58
**ESA** European Space Agency . . . 2
**EW** Extra-Wide Swath mode . . . 12
**FFT** fast Fourier transform . . . 61
**GEE** Google Earth Engine . . . 17
**GMES** Global Monitoring for Environment and Security . . . 2
**GRD** Ground-Range Detected . . . 10
**GrIS** Greenland Ice Sheet . . . 13
**HH** horizontal-horizontal . . . 14
**HV** horizontal-vertical . . . 14
**ICC** incoherent cross-correlation . . . xv
**InSAR** Interferometric Synthetic Aperture Radar . . . xii
**IW** Interferomatric Wide Swath mode . . . 2
**OLI** Operational Land Imager . . . 14
**RBIS** Roi Baudouin Ice Shelf . . . xi
**SAR** Synthetic Aperture Radar . . . xi
**SLC** Single Look Complex . . . 10
**SM** Strip Map mode . . . 12
**TOPSAR** Terrain Observation with Progressive Scans SAR . . . xi
**VH** vertical-horizontal
**VV** vertical-vertical
**WV** Wave mode . . . 12

# 1 INTRODUCTION

The cryosphere is an essential component of the Earth's climate system. It has received increasing attention in the past years mainly because of the mass loss that contributes to sea-level rise [Church et al., 2011], which in turn has an impact on the global environment and on the human society [Rees, 2011].

Although it is not a determinant factor to sea-level rise, the mass loss of the Antarctic and Greenland ice sheets is undergoing an acceleration [Rignot et al., 2011b]. This accelerating mass loss may be dominant to sea-level rise in the future [Meehl et al., 2007]. As the largest ice body on Earth, the Antartica Ice Sheet (AIS) contains an ice volume of 27 million $km^3$, equivalent to 58$m$ potential sea-level rise [Fretwell et al., 2013]. 74% of its coastline is surrounded by ice shelves, the extensions of land ice floating in the ocean [Bindschadler et al., 2011]. These ice shelves play an important role in controlling the stability and regulating mass balance of the ice sheet via the buttressing effect [Dupont and Alley, 2005; Rignot et al., 2013]. The loss of these ice shelves may lead to a considerable discharge of the grounded ice [Rignot, 2004]. For this reason, it is important to observe the evolution of the Antarctic ice shelves, in order to assess the status and change of the AIS and its impact on a global scale.

## 1.1 PROBLEM STATEMENT AND MOTIVATION

In recent decades, multiple ice-shelf collapses have been observed in Antarctica, among which Larsen A (1995) and Larsen B (2002) are documented and related to surface meltwater [Banwell et al., 2013]. Although the cause of the recent calving event of Larsen C (2017) remains unknown, the mechanism of water melting and ponding has been proposed as a possibility [Hogg and Hilmar Gudmundsson, 2017]. Meltwater that leads to these abrupt ice-shelf losses has the characteristic of being intense, extensive or prolonged [Luckman et al., 2014]. It usually percolates into the firn layer, an intermediate between snow and ice, where it refreezes into ice due to a lower temperature, and then densifies the firn, saturates it, and releases heat to the layer [Ligtenberg, 2014; Luckman et al., 2014]. Once the water cannot be accommodated, it may form lakes, and eventually drain towards the ocean [Ligtenberg, 2014]. The drainage changes the stress within the lakes' coverage, and results in a collapse in the ice sheet [MacAyeal and Sergienko, 2013]. Therefore, it is important to carry out thorough studies on the meltwater phenomenon on the Antarctic ice shelves.

While the above process has been frequently recognised in Greenland and the Antarctic Peninsula, the surface mass in East Antarctica has been generally assumed to be stable. However, a recent research [Lenaerts et al., 2016a] revealed the existence of well-formed meltwater streams and storage on Roi Baudouin Ice Shelf (RBIS), Dronning Maud Land, East Antarctica. A part of the meltwater storage is in the form of lakes under the surface, which is unprecedented in this part of the continent. One of the lakes reported is located about four metres under the surface, with the depth of several metres, and the diameter of approximately one kilometre. This finding indicates a potential vulnerability of East Antarctica in the following perspectives: 1) as is mentioned above, the englacial refreezing process of meltwa-

ter transmits heat, enters the sub-shelf cavity and enhances basal melting rates, and 2) future climate change may give rise to water drainage in this area, causing the similar collapse as the ice-shelf calving events that have happened in the Antarctic Peninsula [Lhermitte, 2017].

Compared to the existence of surface meltwater in East Antarctica that has been reported and observed in a previous research [Langley et al., 2016], the knowledge of the subsurface meltwater is limited. Currently, one of the lakes has been studied by the *in situ* observation and measurement using ground-penetrating airborne radar [Lenaerts et al., 2016a]. However, due to the strong melting events on the ice RBIS, not all the subsurface features can be visited, therefore a novel and reliable method to study these features is required.

To select the method, several limitations should be considered. First, the remote location of Antarctica limits continuous *in situ* observation. Although the subsurface melt features may give certain surface anomalies, and these anomalies can be revealed by optical images, few optical images are valid due to the cloud cover and polar night [Luckman et al., 2014; Langley et al., 2016]. In addition, the probability that the subsurface features remain completely hidden should not be neglected, hence a sufficient penetration depth through the firn layer is required. Because the physical environment of Antarctica changes rapidly, it is also ideal to have a relatively high spatial and temporal resolution to capture as much information as possible.

Over the past years, a number of researches with the purpose of observing and monitoring the ice sheet adopting SAR have been carried out in Greenland [Johansson and Brown, 2012; Miles et al., 2017], where the limitations are similar to Antarctica. The previous researches usually applied the amplitude of SAR, with/as the complement of the optical images. For detecting both the occurrence of melting and dynamic changes, these studies required abundant optical images within a certain epoch. But the optical images may not be sufficient in Antarctica. Therefore, this study aims to further apply the information provided by SAR by involving interferometry. The InSAR technique can be used to assess and measure the dynamic processes happening in a certain region, and the existence and evolution of the lakes are two of the processes that are expected to be captured. By using the technique, it may not be a problem if the optical images are not available. With the advantage and potential shown in Johansson and Brown [2012], the use of Sentinel-1 has been recommended.

Sentinel-1 is within the frame of the Global Monitoring for Environment and Security (GMES) Space Component programme undertaken by the European Space Agency (ESA) [Torres et al., 2012]. It applies C-band, which has a wavelength of approximately 5.6cm, thus a penetration ability of several metres into ice and snow; this is theoretically sufficient for the detection of the subsurface water features [Miles et al., 2017]. The coverage of the Sentinel-1 system is considerably wide, with up to 250$km$ under Interferomatric Wide Swath mode (IW), and the spatial resolution is moderate as $20m \times 5m$ [Torres et al., 2012; Yague-Martinez et al., 2016]. Its constellation involves two polar-orbiting satellites, each with a 12-day revisit time [Torres et al., 2012]. And in the acquired signals, both amplitude and phase information are preserved. These concepts and technical parameters will be demonstrated further in Chapter 2. One additional advantage of the Sentinel data is that they are provided as open source.

In addition, although this research is specifically interested in a relatively isolated and purely natural region on Earth instead of an urban area, the InSAR technique has been actively applied to measuring urban developments such as tunnels and

terrain deformations [Normand and Heggy, 2015; Barla et al., 2016]. Compared to the urban environment, the ice shelf is highly dynamic, thus the study is expected to exploit the potential of InSAR applications under more dynamic circumstances. On the other hand, the observation of the natural phenomenon can be a helpful reference in spatial decision making, which is also important in the Geomatics field.

## 1.2 RESEARCH OBJECTIVES

With the background and related work introduced above, it would be ideal to be able to observe the subsurface meltwater in Antarctica. But the first step of this topic, is to detect these features in a rather small scale, therefore the study takes data over East Antarctica. The research questions are thus specified as follows:

*To what extent is InSAR capable of detecting subsurface meltwater in East Antarctica?*

To answer this, the following sub-questions are to be covered:

- To what extent can InSAR observe the temporal behaviour of the subsurface meltwater?
- What is the optimal method to apply the InSAR images to detecting subsurface meltwater?
- How well can InSAR technique perform in polar areas in comparison to other satellite remote sensing methods (optical remote sensing and pure amplitude information)?

## 1.3 SCOPE AND CONTRIBUTION

In the following chapters, the research objects and process of this thesis will be presented. Chapter 2 first introduces the phenomenon to be studied, *i.e.* how the meltwater features are formed, and then sheds light on the remote sensing technique, InSAR, or more specifically interferometry with Sentinel-1, to study this phenomenon. Chapter 3 will briefly introduce the data acquisition, and step further to describe the processing of Sentinel-1 InSAR data, and how to analyse and utilise the outcome. Chapter 4 will give the final results and analysis. Finally, Chapter 5 will conclude the performance provided by this study, and give recommendations on future work. Supplementary images are added in Appendix A when they help with the understanding of the contexts, but are not directly connected to the flow of this document.

Because the main focus of this study is to discuss the feasibility of applying InSAR for subsurface meltwater detection, instead of developing a solid InSAR processing algorithm, the optimisation or invention of InSAR algorithms will not be covered.

With this thesis, the author hopes to study the processing and analysis of InSAR data, and add the outcome to the existing methods for glacial studies. If valuable results arise from this thesis, it is thus expected that the method can be used broadly in other regions.

# 2 THEORETICAL BACKGROUND AND RELATED WORK

## 2.1 THEORETICAL BACKGROUND

### 2.1.1 Regional environment

Lenaerts et al. [2016a] explained the melting events on Roi Baudouin Ice Shelf (RBIS). Surface and subsurface melting features tend to occur along the grounding zone of the RBIS. This originates from the surface-based temperature inversion and the topography. The temperature inversion in Antarctica is caused by a larger emissivity of the snow surface than that of the atmosphere [Hudson and Brandt, 2005]. The local topography generates katabatic winds, which lead to a disruption of the temperature inversion, raising the surface temperature on the ice shelf (Figure 2.1a). An increased surface temperature causes the melt of snow, which increases the grain size, hence decreases the albedo [Chu, 2013]. The winds also cause an erosion to the snow on the surface, exposing the ice underneath, which has a lower albedo as well. A low albedo results in an increased absorption of solar radiation (Figure 2.1b) [Lenaerts et al., 2016a]. In general, the melting mechanism is in a positive-feedback manner, which keeps increasing meltwater production in this area (Figure 2.1c) [Chu, 2013].

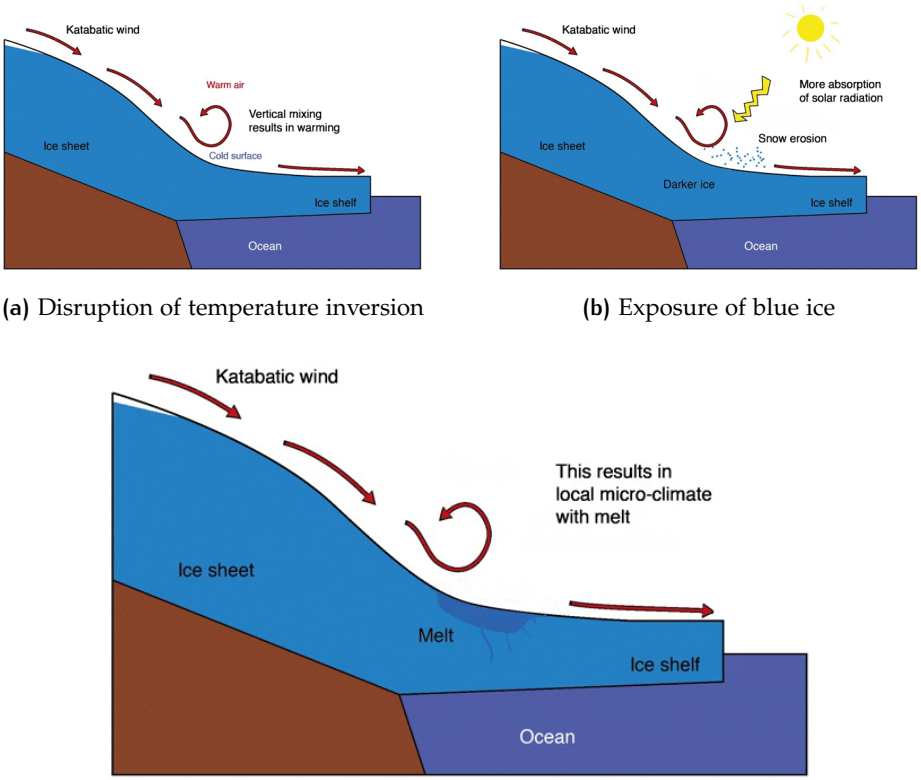


**(a)** Disruption of temperature inversion

**(b)** Exposure of blue ice

**(c)** Melting

**Figure 2.1:** Melting process caused by the local micro-climate (credit: S. Lhermitte; figures from Mooney [2016])

With this information, it is expected that the meltwater features should be found along the grounding line of the RBIS. Therefore, this research will specifically focus on this type of region. In addition, the lakes are initially on the surface, hence as they melt and refreeze over time, they can switch between surface lakes and subsurface lakes, which is a characteristic to be noted [Lenaerts et al., 2016a], because this can influence the interpretation of the InSAR images, specifically the amplitude and coherence (Subsection 2.1.2). Figure 2.2 shows two available Landsat images taken on Dec. 19, 2017 and Jan. 11, 2018 respectively. They reveal different extents of melting on the eastern edge of the RBIS.

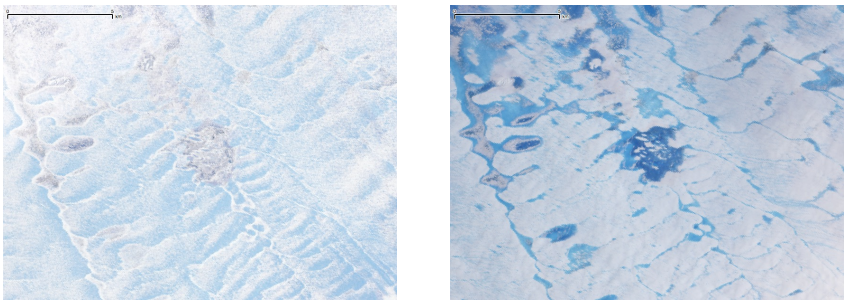

**(a)** Dec. 19, 2017 **(b)** Jan. 11, 2018

**Figure 2.2**: RGB images from Landsat 8

While melting is a behaviour more expected in this studied area, the collapse of lakes can also be observed. From optical images, the collapsed surface tends to be rougher than before, as can be seen from Figure 2.3. The central feature is a lake that experiences a collapse. This collapse may cause a change in elevation, which is expected to be observed from an interferogram (S. Lhermitte, personal communication, Mar. 1, 2018).

Apart from the local behaviours along the grounding line, a global ablation also occurs over the ice shelf. This ablation can be represented by ice velocity, and the magnitude and direction is influenced by factors such as topography and wind. Additionally, these factors interact with each other, forming a complex environment. Therefore, apart from the temporal scale change, the lakes may also have a certain displacement with the ice flow over time (supplementary information of Lenaerts et al. [2016a]). Figure 2.4 shows the DEM over the region of interest [Lenaerts et al., 2016b], and according to Lenaerts et al. [2016a], the dominant wind direction is westward, with an average annual speed of approximately $10 m/s$.

Rignot et al. [2011a] and Mouginot et al. [2012] used mutiple sources of InSAR to measure the ice velocity over Antarctica between 1996 and 2016, and produced an ice velocity map with a $450m \times 450m$ resolution and a unit of $m/year$, in the projection of Antarctic Polar Stereographic (EPSG:3031)[1] [Rignot, 2017]. The statistics and colour map over the RBIS are shown in Figure 2.5. The arrows in the figure [2] represent the direction and scale of the annual displacement, and the velocity down-sampled to $1800m \times 1800m$ for visualisation. If displacements of the lakes occur, this ice velocity information may be used as a reference. From this figure, it can be seen that the displacement should be towards the ocean.

1 The maps in this document, if not specified otherwise, are all in EPSG:3031

2 Discrepancy in the coastline and the outlines of the ice velocity map may be caused by different data sources and dates of acquisition.

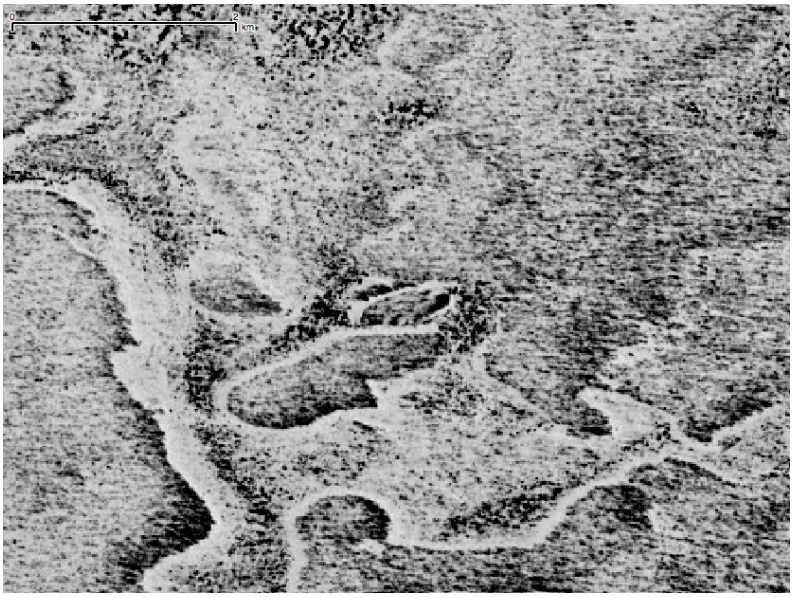

**(a)** Dec. 1, 2017

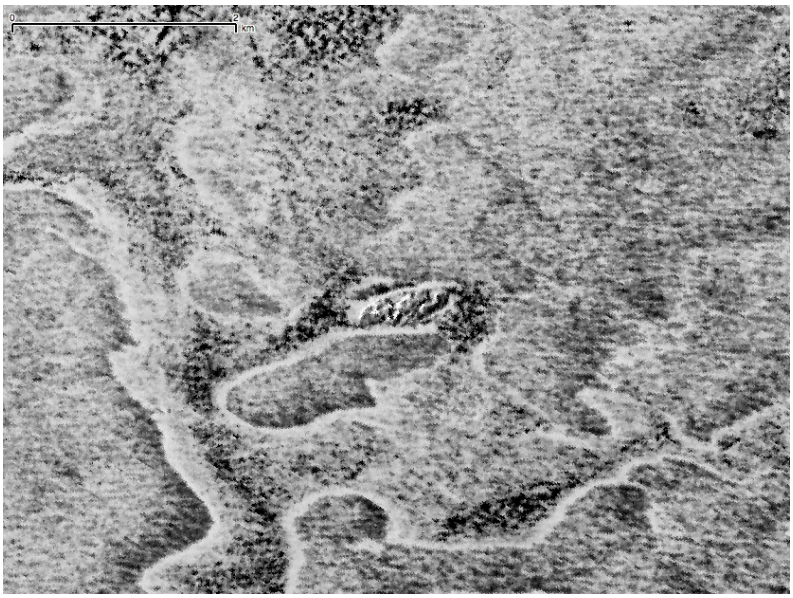

**(b)** Dec. 19, 2017

**Figure 2.3:** Panchromatic images from Landsat 8

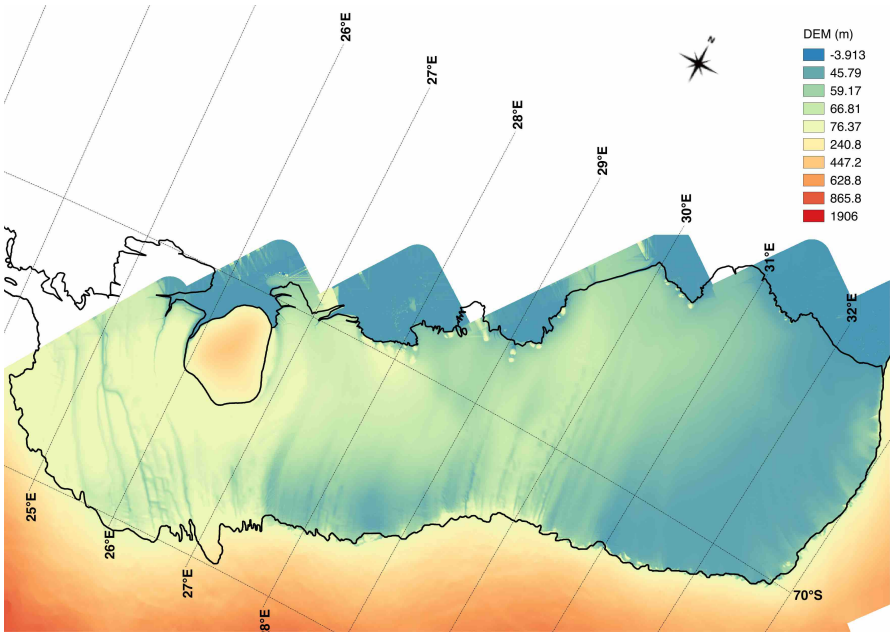


**Figure 2.4:** DEM over part of the RBIS (coastline map from SCAR Antarctic Digital Database [2016]; visualised by QGIS [QGIS Development Team, 2017])

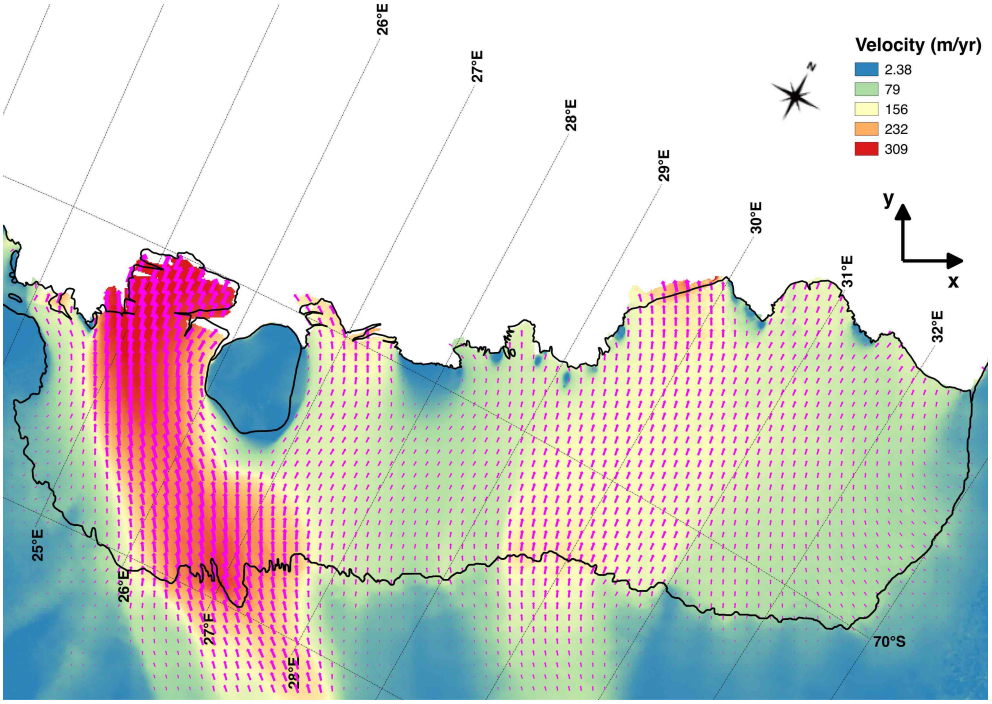


**Figure 2.5:** Ice velocity over the RBIS

### 2.1.2 SAR Interferometry

Figure 2.6 gives the geometric concepts of a SAR system. The along-track direction is the azimuth and the across-track direction is the range. The electromagnetic waves emitted by the satellite travel along the slant range and take the measurement on the ground. Then they are backscattered and recorded within pixels.

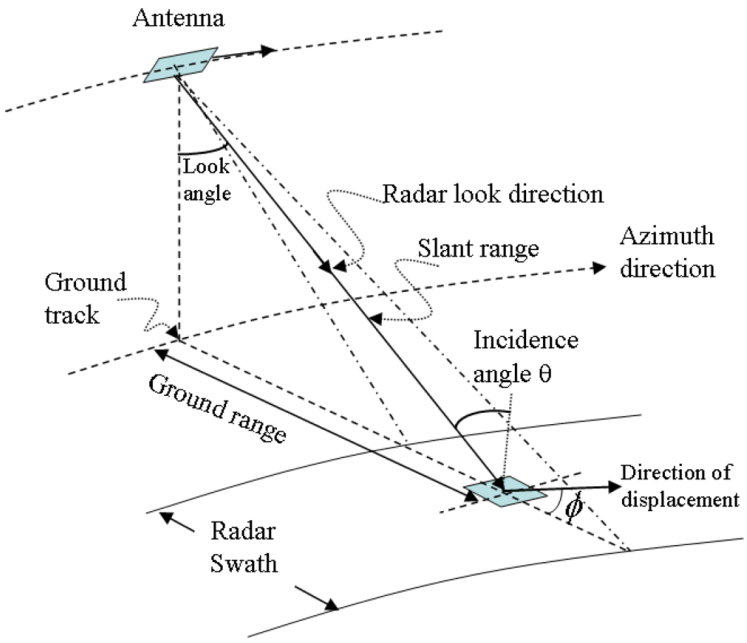


**Figure 2.6:** Geometric concepts of SAR [Zhou et al., 2009]

The basic components of an InSAR image pixel are amplitude and phase. For each pixel, the signal of it can be expressed as [Beckmann and Spizzichino, 1987]

$$z = \sum_{k=1}^{N} A_k e^{j\phi_k}$$

where $A_k$ refers to the amplitude and $\phi_k$ is the phase of each individual scatterer. This can also be expressed in the complex form

$$z = x + jy$$

where the amplitude is computed as

$$A = \sqrt{x^2 + y^2} = |i| \tag{2.1}$$

and phase

$$\phi = arctan2\left(\frac{y}{x}\right) \tag{2.2}$$

In the InSAR signal, the amplitude represents the strength of the reflected signal, and the phase is the received fraction of a complete wave cycle [SkyGeo, nd]. Both types of information are needed for this research. An InSAR dataset $i$ is a complex array of $z$.

The reflection depends on surface roughness, incidence angle and dieletric property. For a region covered by snow, ice and water, this means that the different facies can be roughly distinguished by the amplitude of the recorded signal in an InSAR image. As will be mentioned in Section 2.2, Miles et al. [2017] detected the subsurface

lakes with amplitude information, defining them as small, dark areas appearing in Sentinel-1 Ground-Range Detected (GRD) imagery. But the amplitude criterion can vary over time [Adodo et al., 2017].

The previous studies mainly focused on the different behaviours of water, ice and snow when interacting with microwave, which are expected to be reflected in the amplitude of the Sentinel-1 imagery. A smooth water surface would give low backscatter, while a rough water surface influenced by wind may appear brighter [Luckman et al., 2014]; dry snow gives higher backscatter due to volume scattering, while wet snow may be darker depending on the absorption of the water content [Kunz and Long, 2006]. And according to Hirose et al. [2008], a thin ice layer on top of water gives a low backscatter, because the microwave either penetrates the ice and gets absorbed by water, or be reflected in the direction away from the sensor. As the ice layer increases, the congealed ice may give rise to bubble contents, thus increasing the backscatter. As long as the water freezes through, the ice/water interface may become new ice/old ice interface, which leads to a decreased dielectric difference. In this case, the backscatter drops again.

With two Single Look Complex (SLC) images, which are referred to as master and slave images respectively, an interferogram can be formed by the following computation [De Zan et al., 2015]

$$I_{12} = |I_{12}|exp(j\varphi_{12}) = \overline{i_1 i_2^*} \tag{2.3}$$

and this result provides the information of coherence and phase, computed with

$$coh_{12} = \left| \frac{I_{12}}{|i_1||i_2|} \right| \tag{2.4}$$

$$\phi_{12} = arctan2\left( \frac{I_{12}}{|i_1||i_2|} \right) \tag{2.5}$$

The coherence between InSAR images depends on a series of factors including perpendicular baseline, surface movements, and volume [Zebker and Hoen, 2000] in the environment of snow and ice. Usually, the coherence is an indicator of the quality of the interferogram, where a high coherence *i.e.* good quality refers to clear fringes. From these fringes, the movement of ice as well as the topography can be revealed.

Figure 2.7 is an example of the combination of interferogram fringes and amplitude. This image is processed by Delft Object-oriented Radar Interferometric Software (DORIS) [TU Delft Radar Group, 2017], over the eastern side of the RBIS. The slave date is 10/09/2016 and the master date 22/09/2016, taken from descending track No. 136. A clear low amplitude in the middle-to-lower-right part of the image shows the grounding area, where severe melting events and craters were found [Lenaerts et al., 2016a]. The melting events result in the exposure of blue ice and water, which contributes to this low amplitude. Fringes on the left of the image are dominated by ice movement, while fringes on the right mainly show the topography. In general, the fringes are consistent and clear, which means that the coherence in this area within this period is relatively high. For ice velocity, the denser fringes indicate a larger displacement. This corresponds with Figure 2.5. The ocean is in the dark upper-left part of the image, with some fringes showing stable sea ice.

Additionally, this research will take into consideration the possibility to distinguish subsurface meltwater with phase inconsistency. This needs the concept of phase

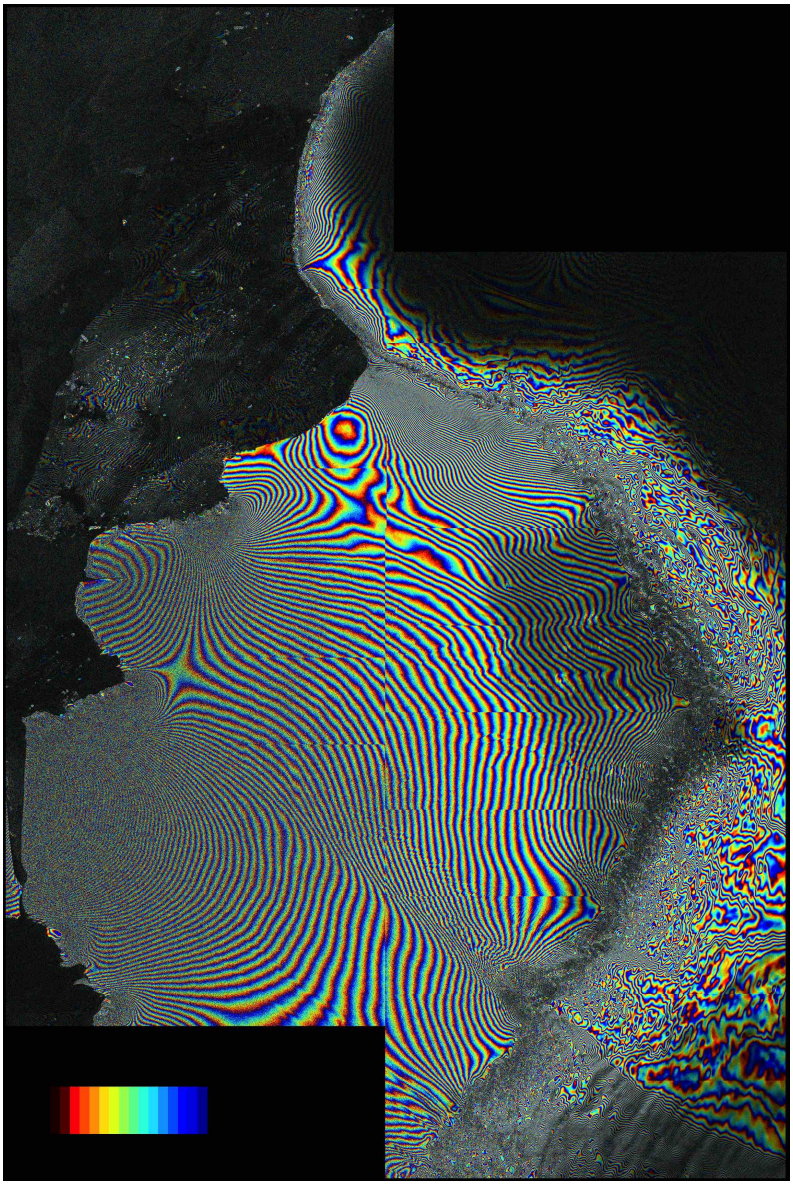

**Figure 2.7:** Example of interferogram

closure. With two slave images and a master image, the phase closure is derived from the interferograms as [De Zan et al., 2015]

$$\Phi_{123} = \phi_{12} + \phi_{23} + \phi_{31}$$

and is expected to be zero. If it is not the case in the image, it could be presumed that the microwave has been influenced by volume scattering. But due to the complex and dynamic local environment, it is also likely that the phase inconsistency cannot be properly interpreted. An example is shown in Figure 2.8, where ice, dry snow, wet snow, and surface and subsurface melt coexist. In this kind of complex environment, the phase inconsistency is rather intense. This image is one of the bursts (to be explained in the following subsection) in the region of interest, and the acquisition of the three images is between 30/08/2017 and 23/09/2017, with a time interval of 12 days.

In this study, the features of the InSAR information mentioned above are expected to be able to indicate the existence of the subsurface water features. However, this is a relatively new concept of which the application has not been thoroughly exploited. Difficulty may arise while interpreting and adopting it.

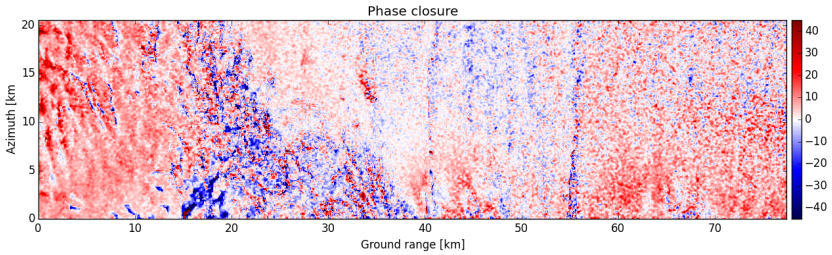


**Figure 2.8:** Example of phase closure

### 2.1.3 Sentinel-1 basics

The data used for InSAR processing are obtained with Sentinel-1, an improved mission compared to the ERS-1/2 and ENVISAT Advanced SAR (ASAR) in the sense of temporal resolution and spatial coverage [Torres et al., 2012]. Its constellation is polar-orbiting, with two satellites in the same plane. An image is recorded every time the same location is revisited by the satellite. The interferometry is hence referred to as repeat-pass.

For each satellite (Sentinel-1A/1B), the revisit time is 12 days. If they both record, the data will have a 6-day temporal resolution. Besides the aforementioned Interferomatric Wide Swath mode (IW) mode, it has three other acquisition modes known as Extra-Wide Swath mode (EW), Strip Map mode (SM) and Wave mode (WV), each with a specific ground coverage and resolution (Figure 2.9). They provide data in SLC and GRD types. The SLC products keep the phase and amplitude, while the GRD products take the spatial average (multilook) of the amplitude. SLC is used for interferometry.

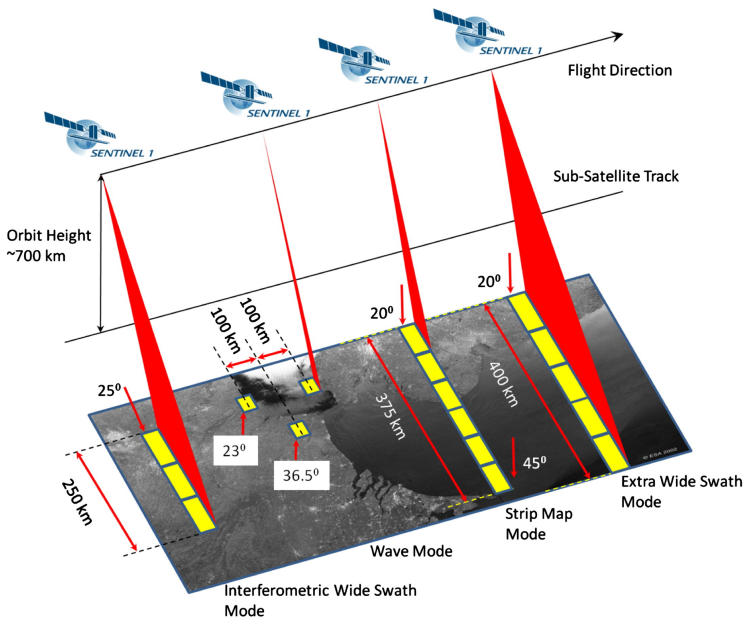


**Figure 2.9:** Sentinel-1 acquisition modes [ESA, 2018a]

This study only applies IW data. This mode provides data with a spatial resolution of $5m \times 20m$ (range and azimuth), and consisting of three sub-swaths acquired with Terrain Observation with Progressive Scans SAR (TOPSAR) technique. Within each sub-swath, sequences of echoes are acquired, which are defined as bursts [De Zan

and Monti Guarnieri, 2006]. TOPSAR is a technique where the scanning beam is not only steered in range, but also rotated from backward to forward of each single burst in the azimuth direction [ESA, 2018a]. With this technique, the images have a lower azimuth resolution, but a larger swath coverage and better suitability for interferometry computation.

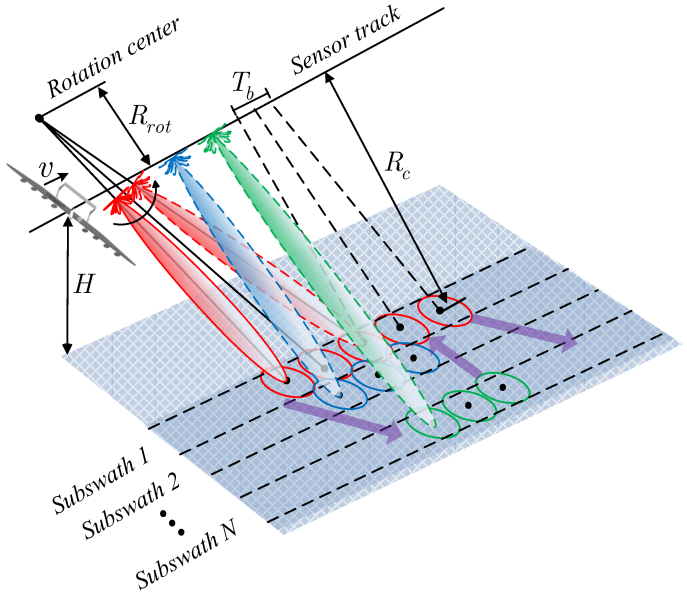


**Figure 2.10:** Scanning mechanism of TOPSAR [Zhou et al., 2009]

With such acquisition mechanism, the InSAR images in this document are indexed by swaths and bursts (Figure 3.2), and their axes, if not georeferenced, are referred to as range (x-axis) and azimuth (y-axis). Their coordinates are defined as line (in azimuth) and pixel (in range). Figure 2.7 shows clearly two swaths horizontally, and the multiple 'blocks' in the vertical direction are bursts. The horizontal lines in between of the bursts are the boundary lines. The lines are clearer on the ice shelf than the ocean and the interior because of the along-track motion *i.e.* inhomogeneous ice flow [De Zan et al., 2014]. This is also obvious vertically, as a line in the middle clearly separates the two bursts. And Figure 2.8 gives the range and azimuth coordinates within one burst.

The acquisition is also specified by ascending track (satellite moving south to north) and descending track (north to south). The example in Figure 2.7 is acquired from a descending track. The fly direction is thus reflected from the image as top-to-bottom, and the look direction is from right to left. On the contrary, Figure 2.8 is acquired from an ascending track, and the orientation of the image is denoted by the axes.

## 2.2 RELATED WORK

Although the research of Lenaerts et al. [2016a] was the first time that such subsurface water features had been found in East Antarctica, the same phenomenon had been spotted and observed in Greenland Ice Sheet (GrIS) and several ice shelves in West Antarctica [Hubbard et al., 2016], and different remote sensing instruments had been used for the observation. Koenig et al. [2015] applied airborne radar in ultra-wideband to detect the ice-water interface based on the difference between the dielectric constants of the two media. Supportive visible-band imagery was also

used to examine surface features that indicated the presence of the meltwater underneath.

Another research to monitor surface and subsurface lakes on GrIS [Miles et al., 2017] applied Sentinel-1 in combination with Landsat 8 Operational Land Imager (OLI) imagery. Regarding the application of Sentinel-1, the data used was Level-1 images in the category of GRD product from the EW acquisition. This type of data has a broad coverage with medium spatial resolution, lacks phase information, and is georeferenced and time-tagged [ESA, 2018b]. Dual-polarisation images (horizontal-horizontal (HH) and horizontal-vertical (HV)) were used to compensate for each other. Based on the characteristics of the data, only the magnitude of the images was analysed, therefore the areas of low backscatter, *i.e.* appearing dark in the Sentinel-1 imagery, and invisible in the Landsat imagery, were directly defined as subsurface lakes [Miles et al., 2017].

The aforementioned two methods are compared in Miles et al. [2017]. The advantage of the method in Koenig et al. [2015] is that the lake depth could be determined because of the sufficient L-band penetration. But the spatial and temporal coverage of the radar restrains the areal measurement and observation during winter. The Sentinel-1 EW GRD measurement by Miles et al. [2017] has an advantage in this aspect. There is a discrepancy of the time of lake presence between the two different researches, and it could be caused by the difference in penetration depths.

The study of Tian et al. [2016] to automatically recognise surface lakes over the Tibetan Plateau used both amplitude and coherence from SAR images. It has provided valuable insights on the possibility of involving more SAR information for water body detection, especially by providing the evidence that water bodies appear darker than the surroundings in a coherence image. Antonova et al. [2016] carried out the observation of thermokarst lakes in Lena River Delta by using both amplitude and coherence information from TerraSAR-X. The observation is based on the theory that the floating ice has stronger backscatter than the ice frozen-through, while the coherence gives an approximately opposite result.

With respect to the RBIS, ground penetrating radar was adopted for depth measurement [Lenaerts et al., 2016a]. By observing the radar cross-section, the upper and lower boundary of the subsurface lakes could be recognised. However, it has the same spatial and temporal restrictions as the ones in Koenig et al. [2015].

While the amplitude information shows a promising result in the study of Miles et al. [2017], it also depends highly on the snow profile. Adodo et al. [2017] studied the seasonal change of backscattering coefficient over the Antartica Ice Sheet (AIS) with three bands of radar altimetry. The bands are S-band, Ku-band and Ka-band. It was concluded from this study that the backscattering of different frequencies can be influenced by different factors such as temperature, grain size, snow density, surface roughness and wind speed. Generally, it was implied that the seasonal variation at S-band was dominated by surface properties, at Ka-band was mainly due to the volume echo, and at Ku-band had the influence from both of the factors [Adodo et al., 2017]. C-band, with the wavelength between S-band and Ku-band, might have a backscattering variation mainly driven by the surface echo. However, conclusion could not be drawn how exactly snow properties influence the S-band backscatter because of the complexity of the mechanism and a lack of information on the snow roughness [Adodo et al., 2017]. It could then be inferred that it may not be simple to interpret the C-band backscatter variation as well.

The studies using InSAR were usually carried out with the aim of mapping glacier surface displacement. Conservatively, by analysing the phase coherence in the inter-

ferogram generated by two images taken in the same area at different time, the terrain motion can be retrieved [Zebker and Hoen, 2000]. However, in the ice-covered area, a great amount of phase decorrelation can be caused by volume scatter, and this feature is used by Zebker and Hoen [2000] to determine penetration depths of InSAR, as well as by Banda et al. [2013] to analyse subsurface ice structure. De Zan et al. [2015] also proposed the phase inconsistencies for volume detection. Based on these ideas, this project will be carried out with the advantage of Sentinel-1 SLC products, which preserve both amplitude and phase information, in order to explore and apply the potential of InSAR in subsurface water observation on ice shelves.

# 3 METHODOLOGY

With the motivation introduced in Chapter 1, and basic concepts presented in Chapter 2, this chapter aims to elaborate on the work flow, from data acquisition to the final visualisation. Figure 3.1 gives an overview of the main processes. Apart from Delft Object-oriented Radar Interferometric Software (DORIS), the processing is mainly done with Python 3.4 and partly done with MATLAB and Google Earth Engine (GEE), and the visualisation is via QGIS[1].

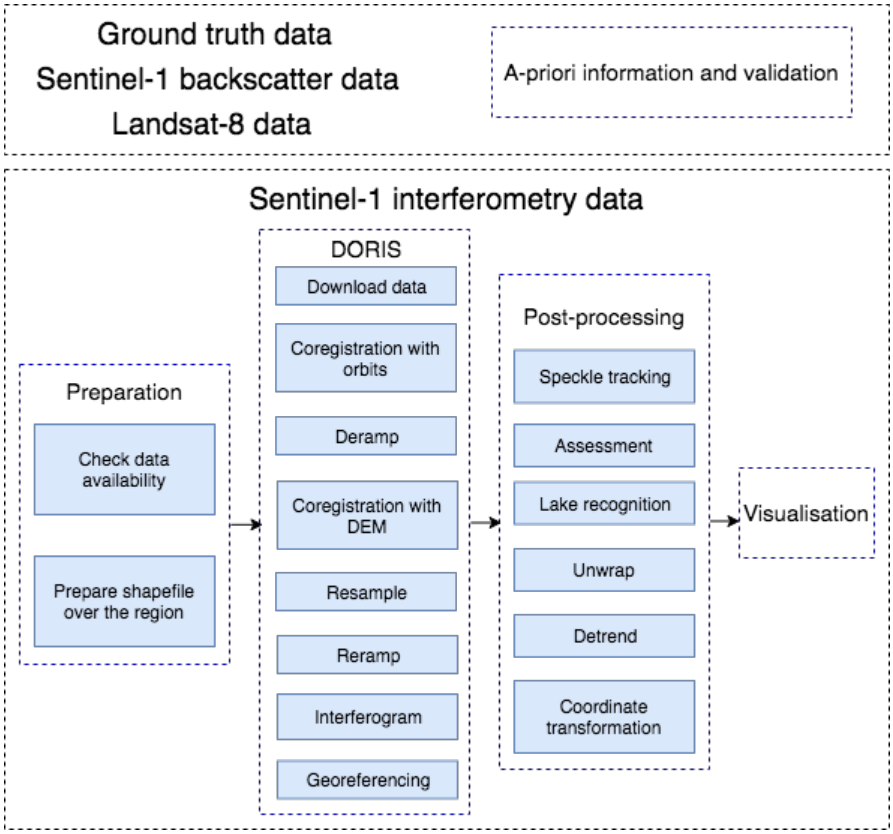


**Figure 3.1:** Workflow of the project

## 3.1 STUDY REGION AND DATA ACQUISITION

### Roi Baudouin Ice Shelf (RBIS)

The Sentinel-1 Single Look Complex (SLC) data are accessible on Copernicus Open Access Hub [Copernicus, 2017]. To study the Roi Baudouin Ice Shelf (RBIS), the available data and the coverage of the acquisitions are visualised in Figure 3.2. Although it is mentioned in Subsection 2.1.1 that the most interested area is the grounding zone of an ice shelf, for RBIS, the starting point is to have an overview of the whole

1 From this chapter, the longitude and latitude grids are left out for clarity.

ice shelf and see how far the micro-climate has influence on.

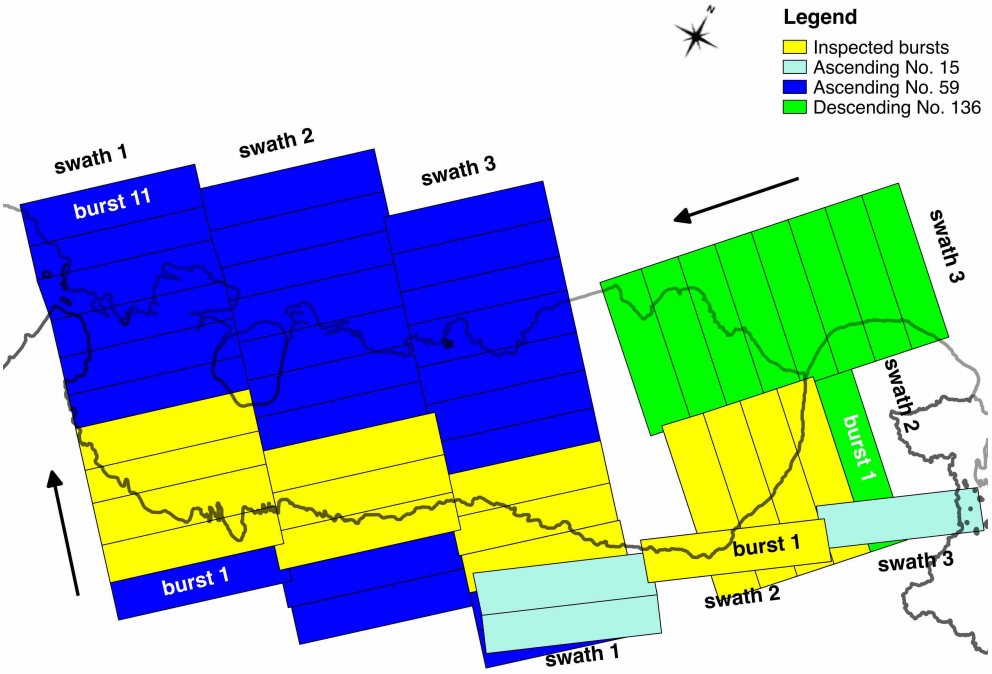


**Figure 3.2:** Coverage of the Sentinel-1 data over RBIS

After defining the region of interest and obtaining the satellite data, a DEM is fed to DORIS to prepare for processing. The DEM provided by Lenaerts et al. [2016b] is generated with TanDEM-X, and has a high resolution of $10m \times 10m$. It has been shown in Figure 2.4.

According to Subsection 2.1.2, to inspect the phase closure, three successive images are needed. These three images are defined as a triplet. Because the local environment changes constantly, to minimise the temporal decorrelation among the three acquisitions, the date in the middle is chosen as the master, and the other two are coregistered to it. Table 3.1 gives the information on the availability of the data. It is noted that since 2015, the data in this region are not regularly available, therefore this study only uses the data that consistently have the shortest revisit time possible.

| Track No. | Starting date | End date | Revisit time | Satellite platform |
|---|---|---|---|---|
| Ascending 15 | 22/07/2017 | 11/02/2018 | 12 days | Sentinel-1A |
| Ascending 59 | 25/07/2017 | 26/02/2018 | 12 days | Sentinel-1A |
| Ascending 59 | 22/03/2018 | 15/04/2018 | 12 days | Sentinel-1A |
| Descending 136 | 04/12/2017 | 15/04/2018 | 12 days | Sentinel-1B |

**Table 3.1:** Data availability in Roi Baudouin Ice Shelf

The orbit information needed for coregistration is downloaded within the specified time period. This information is the precise orbit provided by ESA.

Furthermore, to finally locate the lakes, this study takes the ground truth taken by Lenaerts et al. [2016a] as a reference. One of the lakes has been measured locally (supplementary information of Lenaerts et al. [2016a]), and the others are mapped with a combination of Landsat imagery and Advanced Land Observing Satellite (ALOS) (L-band SAR) data. The ALOS data date back to the summer season (December, January, February (DJF)) between 17/12/2010 and 30/01/2011. Figure 3.3 shows the

mapping of the lakes, in a smaller scale and zoomed in.

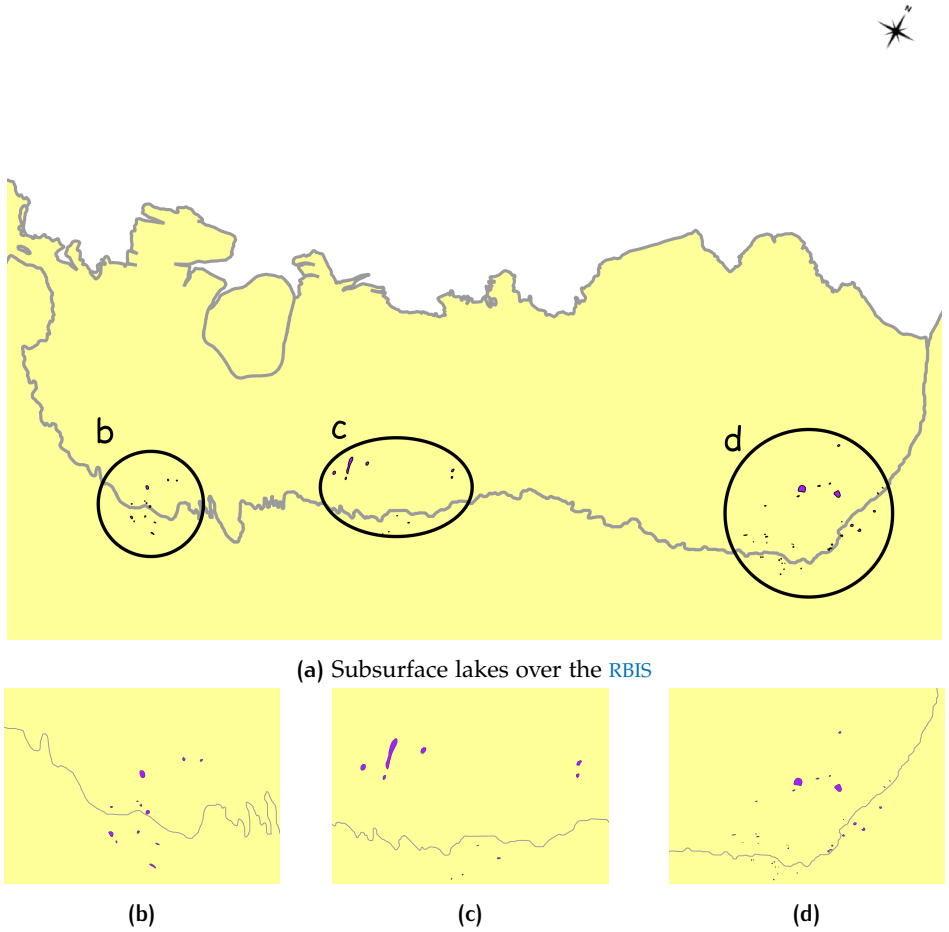


**(a)** Subsurface lakes over the RBIS

**Figure 3.3:** Subsurface lakes mapped by Lenaerts et al. [2016a]

To be able to compare the results from this study with the one of Lenaerts et al. [2016a], the ice velocity map is also a reference, in order to measure the displacement of the lakes. This map is provided by Rignot [2017], and visualised in Figure 2.5.

Additional optical images are downloaded from GEE, as is visualised on the cover. When available, these images may indicate the surface conditions, especially with respect to the extent of melting (Figure 2.2). Because the Sentinel-1 Ground-Range Detected (GRD) products have a better temporal availability than the SLC data, they are taken to study the occurrence and properties of the lakes on GEE as a reference. The weather data between July 2017 and February 2018 are ERA-Interim data [Dee et al., 2011]. They are expected to provide information on the annual variation of local environments including wind speed, air temperature, snow temperature, *etc.*

### Amery Ice Shelf

To apply the InSAR study in a broader scale, the grounding zone of Amery Ice Shelf is taken as another study region. This region shares a similar topography as the RBIS. However, this ice shelf does not have supportive *in situ* data or DEM from TanDEM-X. The mapping of the subsurface lakes may be no more than a repetitive process, but a river was spotted in 2017, and has been expected to be hidden since then (S. Lhermitte, personal communication, Apr. 17, 2018), as is shown in Figure 3.4. The

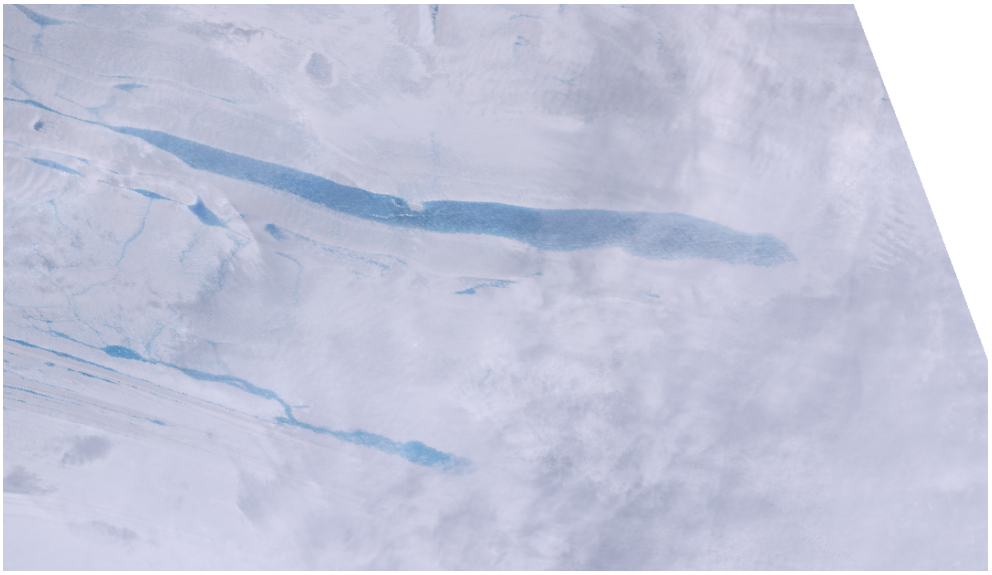

**Figure 3.4:** Landsat image captured over Amery in January, 2017

phenomenon is documented in Kingslake et al. [2017]. Therefore, for this region, the focus is solely on this feature. Because an open water area and an ice cover can be hard to distinguish from optical imagery, as they both show up blue, the validation of this feature is lacking. The spatial and temporal coverage of Sentinel-1 SLC data are shown in Figure 3.5 and Table 3.2.

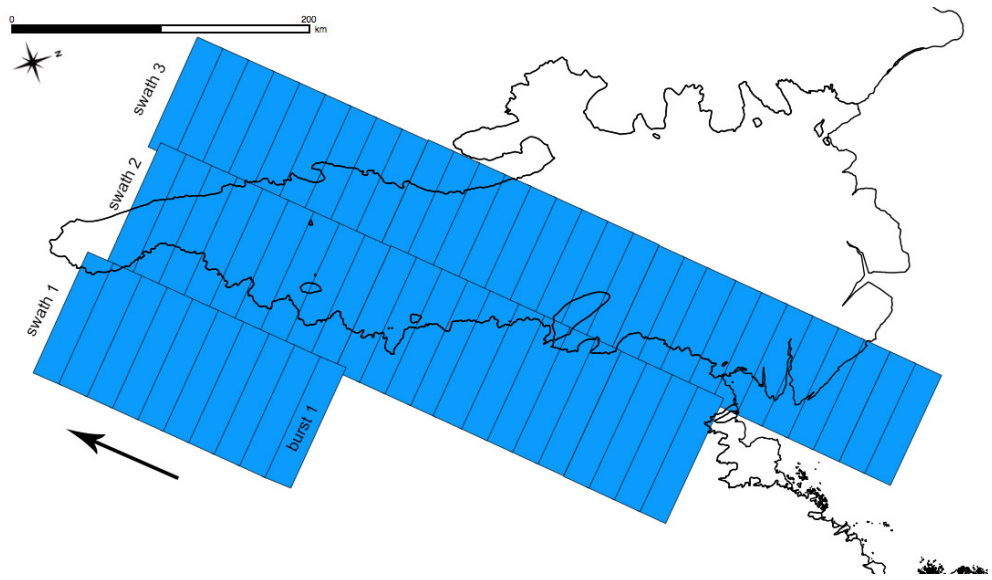


**Figure 3.5:** Coverage of the Sentinel-1 data over Amery

| Track No. | Starting date | End date | Revisit time | Satellite platform |
|---|---|---|---|---|
| Descending 3 | 04/01/2017 | 16/01/2017 | 12 days | Sentinel-1B |
| | 16/01/2017 | 10/05/2017 | 6 days | Sentinel-1A & 1B |
| | 22/05/2017 | 07/09/2017 | 6 days | Sentinel-1A & 1B |
| | 25/09/2017 | 06/03/2018 | 6 days | Sentinel-1A & 1B |

**Table 3.2:** Data availability in Amery Ice Shelf

## 3.2 INSAR PROCESSING

The main steps performed by DORIS are introduced in Appendix B. For further implementation, the valid output files are [Delft Institute of Earth Observation and Space Systems (DEOS), 2008]:

- Data files: the complex data coregistered, resampled and reramped;
- Unwrap input files: the interferogram and coherence processed without filtering or multilooking;
- Reference phases: two separate parameters for flat-earth correction and DEM correction;
- Result files: master and slave results files, where the process control flags and parameters such as two-way data acquisition time, corner coordinates, radar wavelength *etc.*;
- Georeferenced locations: two separate files for longitude ($\lambda$) and latitude ($\phi$) of each point respectively.

Further processing may involve ICC and CCC, as is explained in Appendix C. Their results are also displayed. Because the methods need more optimisation, especially with respect to removal of noise from valid small features, they are not adopted in this project.

With the output data files, the information introduced in Subsection 2.1.2 can be derived.

## 3.3 LAKE LOCATING

To study RBIS, because of a comparatively high spatial and temporal coverage, the data from track No. 59 are chosen to give an overview for selecting the bursts where the strong melting occurs. A detailed description will be presented in Section 4.1.

### 3.3.1 Detection of static occurrence

As Subsection 2.1.2 indicates, water and wet snow tend to appear darker in amplitude than dry snow. When a lake is covered by snow, it may give a melted boundary which is darker than the surrounding snow and the snow-covered centre. When the lake is open, the whole lake can be dark because of the exposure of water. The coherence may be informative as well, generally showing up darker for water bodies in comparison to the surroundings. In this case, a temporal assessment of the amplitudes and coherence will be performed. For the static detection, the dates with relatively high amplitude and coherence will be singled out, because the water features are easy to capture based on the aforementioned criteria. A low amplitude can also be used as a reference to differ lake from snow spots.

Because the static detection focuses on the contrast between the lakes and their surroundings and an uncertainty may be introduced in this way, the central areas of several lakes are first extracted, and the spatial average values of amplitude and coherence within each area are assessed temporally. In this step, it has to be certain that the central areas are water features, hence the *in situ* data and Landsat 8 images are taken as reference. Then, a buffer zone within an angular distance of approximately 0.005 degrees from each central area is defined in this step, their temporal amplitude and coherence assessed as well. This step aims to approximately quantify the contrast between the lakes' centres and the outer areas, especially from a temporal perspective. A larger contrast refers to a smaller uncertainty of locating the lake. The snow and ice in the non-watery area will be assessed in the same way, in order to differ subsurface processes (*e.g.* forming of meltwater) from surface processes (*e.g.* surface melting and motion). These areas are mapped and indexed as in Figure 4.4a and Figure 4.4b.

On the other hand, a spatial delineation of the lakes is done by measuring the backscatter along a certain direction of the lakes and their surroundings. Here, two directions are taken, the criterion being the estimated largest and smallest extents. Because the Sentinel-1 GRD products are more frequently provided within a longer time, it can be more informative to study the variation of amplitudes with these products. These steps not only aim to provide the insight of the lake evolution temporally and spatially, but also give the reference for an advanced static detection of subsurface meltwater when the research area is large, the data are abundant, and the images are multilooked properly.

For visualisation, the bursts are written into *geotiff* format. The details are provided in Appendix B. After all the interested bursts are fitted to the map, the lakes are separated into two groups ready for classification. Because the lake area within ascending track No.59, swath No.1, burst No.3 (indices shown in Figure 3.2) was visited in 2016 and revisited in 2017 (S. Lhermitte, personal communication, Jan. 10, 2018), it is a more reliable reference to check how lakes would show up in different features including amplitude, coherence, phase and closure. With this reference, the characteristics of the lakes are summarised and applied to the grounding zone of the RBIS.

For lake classification, an ideal method is to apply a simple feature recognition with thresholding, region growing, or edge detection by using the characteristics mentioned above. But speckles exist in the InSAR images. For automatic classification, they should be removed properly. This requires a trade-off between the preservation of lake boundaries and sufficient removal of speckles. Another issue is that due to the lack of training data, it may be hard for the algorithm to distinguish lakes from sastrugi. Therefore in this study, the automatic classification is not yet implemented. The lakes are thus mapped manually. This process can be done as such also because of the limitation of valid data. If the amount of data increases, more automatic methods should be developed for further work.

### 3.3.2 Detection of dynamic behaviours

Because the lakes have certain displacements over time, a final step is to compute the displacement with the ice velocity. The results will be compared with the ALOS map, in order to understand the global trend of the evolution of the lakes.

While the static lake detection only applies the most characteristic amplitude and coherence information, the understanding of the evolution of these lakes over time and space should involve all the available images. However, it should be noted that

there are times when the whole region loses coherence, and the coherence images will be full of noise thus not measurable.

For a local evolution, the fringe pattern will be analysed. Figure 2.7 is a high-quality interferogram with relatively smooth and continuous fringes. This is guaranteed because of a fine coherence and few movement anomalies contributing or contradictory to the overall ice flow. When a lake undergoes a distinct filling, drainage, collapse, *etc.*, it may cause an interruption to the fringes. The interruption may appear in two forms:

- The coherence of the lake is too low, so that the fringes become noisy thus indistinguishable;
- The coherence of the lake is sufficient, so that a change of density and/or orientation of the fringes may occur.

To study the instant behaviours of the lakes, it is assumed that all the local behaviours are reflected as a vertical change, in contrast to the global ice movement in an approximated horizontal plane. When the interruption is spotted, it is expected that the vertical displacement can be estimated. The fringes represent the terrain features (movement, topography, *etc.*) in an ambiguous manner, also referred to as wrapped phase. To obtain the unambiguous information, a process called unwrapping is performed. This is done with the software SNAPHU [Stanford Radar Interferometry Research Group, 2003]. Then, a detrending is needed to reduce the overall ice flow and reveal the estimated vertical displacement of the lake. The concept of detrending can be found in Appendix D.

Although there is only a small amount of cloud-free optical images in this region, once the optical images are available, they can be used to validate the outcome.

For the river feature on Amery Ice Shelf, the purpose is to check the temporal behaviour, both in the sense of amplitude and fringe patterns. What is expected in this case is whether the freezing of the feature can be captured.

# 4 RESULTS AND ANALYSIS

This chapter aims at providing the results of this study, and will answer the research questions. First, the output from DORIS over the whole RBIS will be presented. It is supposed to provide an insight on how the ice shelf may appear in amplitude and phase. It also helps to indicate the precise area where melting occurs. For simplicity and a higher spatial resolution, the result of further InSAR processing are performed and depicted at burst level.

After obtaining the processed images, an assessment will be carried out, and valid data for lake detection will be selected. A part of the lakes located in Lenaerts et al. [2016a] is chosen to summarise a general set of characteristics of the subsurface lakes. These characteristics are then applied to all the bursts where melting events occur. Following this process, the lakes will be located. If vertical changes can be spotted, the interferogram fringes will be taken to estimate the displacement and infer the behaviour of the lake. The horizontal evolution of lakes can be analysed by the extent in amplitude and coherence, provided that the amplitude and coherence images have a decent brightness and contrast.

## 4.1 GLOBAL OBSERVATION

First, the outputs are analysed from a global perspective. This provides the overview of the whole ice shelf. However, because different tracks have different availability, taking all of the data may introduce spatial and temporal uncertainties. Therefore, only an optimal track should be taken in this step. According to Figure 3.2 and Table 3.1, the ascending track No. 59 has the largest coverage both spatially and temporally. The lakes whose locations are known are also distributed within its coverage (Figure 3.3b). The analysis of this section thus focuses on this track. The overall variation of amplitude and coherence are visualised in Figure 4.1. These images provide an overview of the local environment, and indicate when the analysis based on amplitude and coherence may not be valid.

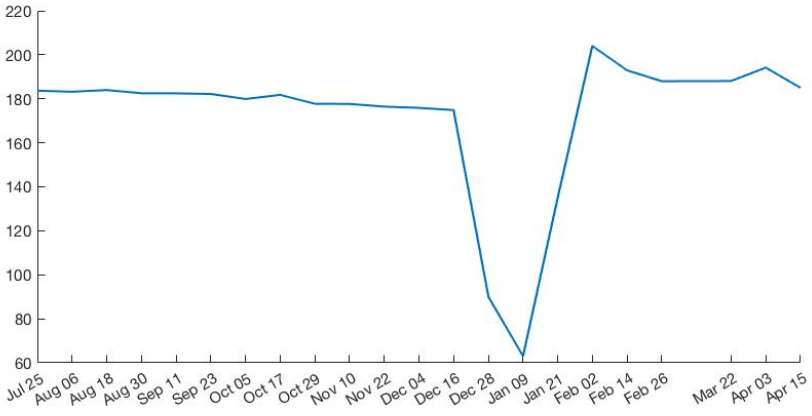


**(a)** Variation of amplitude

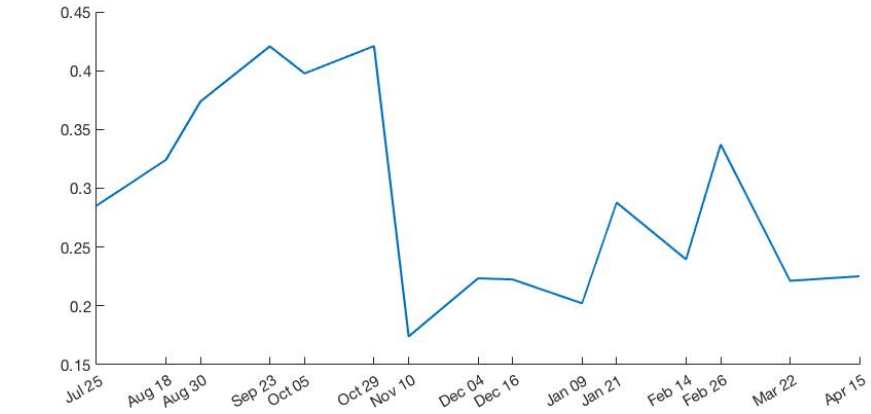


**(b)** Variation of coherence

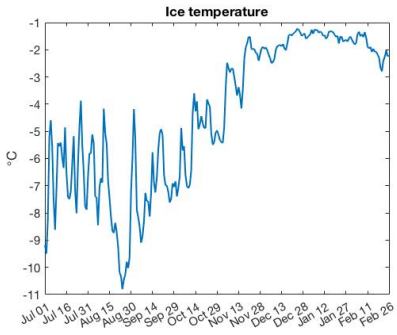


**(c)** Temperature of ice layer

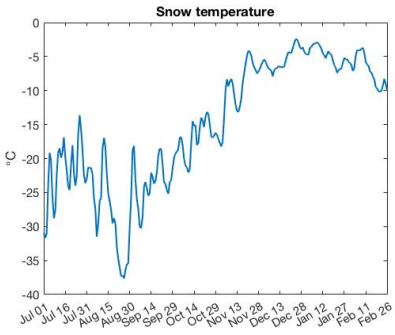


**(d)** Temperature of snow layer

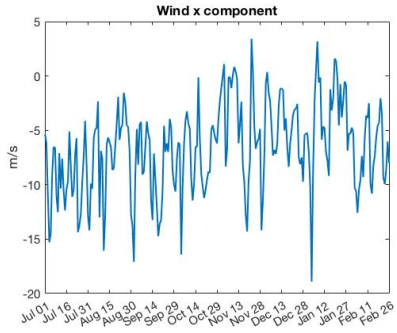


**(e)** Wind velocity in x-direction

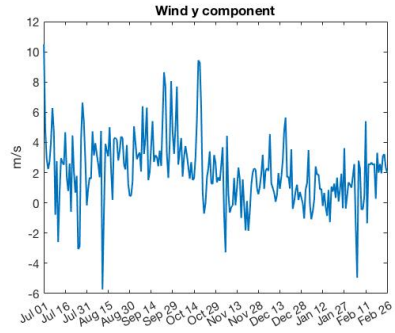


**(f)** Wind velocity in y-direction

**Figure 4.1:** Temporal variation of different properties

A simple assumption has been made that the local temperature and wind speed may influence the amplitude and coherence, because they change the physical characteristics of the surface. The corresponding and available ERA-Interim data are visualised in Figure 4.1. While the high temperatures do have a correspondence with the low amplitude, no solid conclusion of the relation between the physical environment and the SAR image properties can be made from these simple graphs. Moreover, the variation of amplitude and coherence may be influenced by other various factors such as snow density, precipitation and particle size, but these cannot be analysed precisely yet. This study will not discuss the effect the regional environment has on the Sentinel-1 acquisitions in depth. What can be learned from here, however, is that the wind speed does not relate closely to the InSAR observations in this region, whilst the rising temperature indicates that the melt period may have started from mid-November, which might have an impact on the InSAR observation.

Based on Figure 4.1a and Figure 4.1b, the interferogram with phase and amplitude on Oct. 29 (Oct. 17 as master date) is selected to narrow down the melting region

and the result is in Figure A.1. In this region, the overall bright area is the main part of the ice shelf. The fringe patterns are relatively clear because of a regular ice movement. The image appears dark in the regions with exposure of blue ice, which is the region of interest, and also in the regions with rock features. Finally, the bursts selected to inspect the melting are shown in Figure 3.2.

Because the lakes that have been visited are mainly within burst No. 3, swath No. 1, this burst is taken for burst-level analysis in the following sections.

## 4.2 LOCATIONS OF THE LAKES

From Appendix C, the data of this study are only the DORIS output, without further coregistration. Then the amplitude, coherence, phase and closure are computed, and assessed within the full time series regarding their contrast (whether different features can be distinguished) and quality (whether the image is relatively noise-free). There are 6 triplets in the continuous time series of this study, each consisting of 3 amplitude images, 3 coherence images, 3 phase images and a closure image. For simplicity, this document only shows a part of the features that meet/do not meet the criteria for lake detection. And for assessment, no georeference has been performed, which means that the coordinate system is the radar coordinates.

Figure 4.2 gives examples of the images where no features can be extracted. Figure 4.2a is an example where the image has almost no contrast. And in accord with Figure 4.1b, this is the time slot when the coherence dropped drastically. As is introduced in Subsection 2.1.2, a low coherence and a noisy fringe pattern tend to correspond to each other, therefore the simultaneous interferogram is also invalid. Similarly, Figure 4.2b shows a noisy phase pattern. And in general, the phase closures are not valid for detection, because although they may show the outline of the melting region (Figure 4.2c), the overall images are noisy, and it will be hard to justify whether a phase inconsistency is caused by water or other features. The water features are thus not distinguishable.

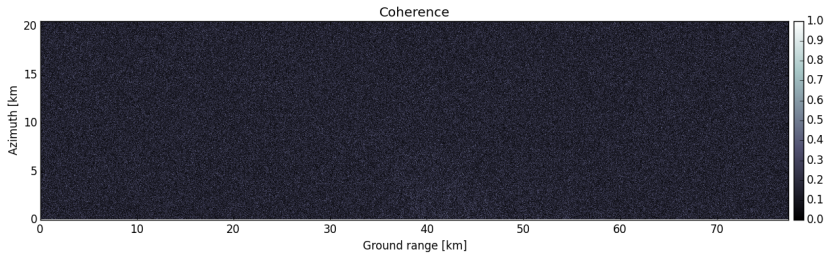


**(a)** Coherence between 10/11/2017 and 22/11/2017

On the contrary, Figure 4.3 shows the images that can be adopted for meltwater detection. Figure 4.3a and Figure 4.3b are the typical amplitude and coherence images where snow features appear brighter while ice and water appear darker. And when the region experiences a strong melting, it can be seen from Figure 4.3c that the amplitude drops, but different features are still distinguishable. For static detection, fringes are not yet considered because the information they provide is similar to coherence images.

The selected features are then projected to the map to further study the appearance and locations of the lakes. Figure A.3 is an overview of the result of the map-

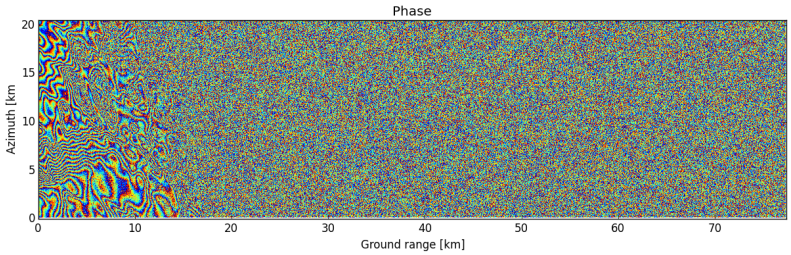


**(b)** Phase between 16/12/2017 and 28/12/2017

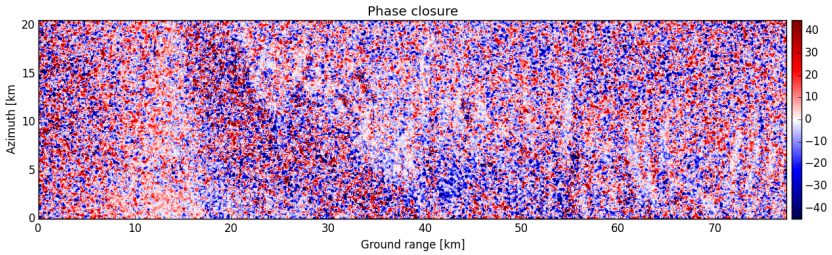


**(c)** Closure between 21/01/2018 and 14/02/2018

**Figure 4.2:** Invalid images

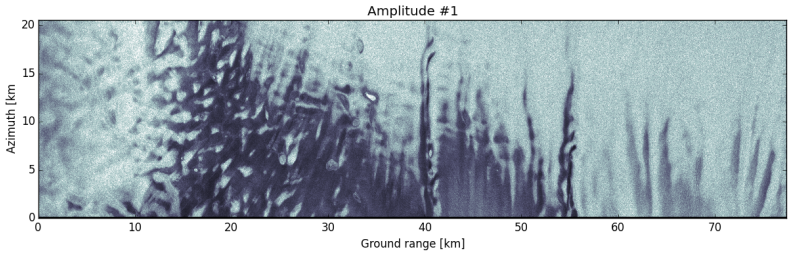


**(a)** Amplitude on 05/10/2017

ping process. In general, the outline of the RBIS from Sentinel-1 processing fits the coastline, showing a relatively reliable georeference from DORIS and post-processing. After all the data are georeferenced, the lakes should be extracted based on the following properties:

- The temporal variation in coherence and amplitude, as well as in comparison with the surroundings, in order to quantify the possible uncertainty of the size of the lakes;
- The temporal variation in coherence and amplitude in the non-lake areas, in order to derive whether there is a strong influence coming from subsurface processes or a pure surface melting;
- The spatial variation in amplitude of the lakes and the surroundings in order to understand the extent and evolution of facies in the lake areas from the first time that the lakes were visited (December 2016); the coherence is not considered spatially because according to the data availability in Table 3.1, the coherence information is relatively insufficient.

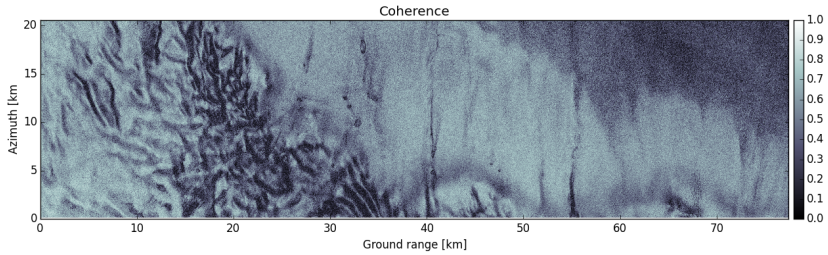


**(b)** Coherence between 05/10/2017 and 17/10/2017

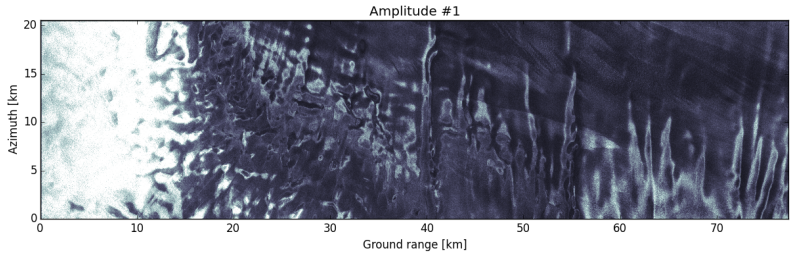


**(c)** Amplitude on 02/02/2018

**Figure 4.3:** Valid images

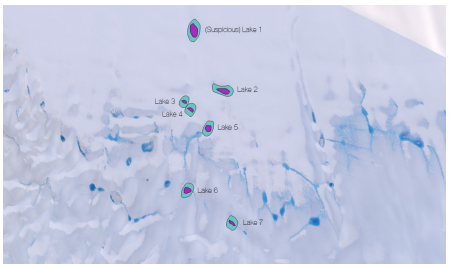


**(a)** Lakes and buffers

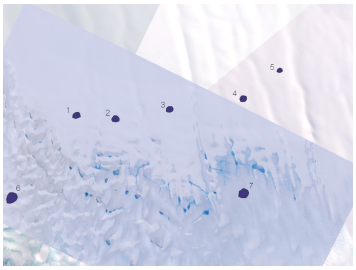

**(b)** Reference areas

**Figure 4.4:** Sample areas for temporal analysis

The methods for the assessments are mentioned in Subsection 3.3.2. And the data used in this step are *in situ* locations of the lakes, Sentinel-1 GRD data and processed InSAR data. The temporal assessments are carried out for the lakes shown in Figure 4.4a and the reference areas in Figure 4.4b, and the spatial assessment is marked in Figure 4.10. The indices of the lakes in Figure 4.4a and Figure 4.4b correspond to each other.

Because the lakes may have a slight displacement over the period when they are studied, and the ice or wet snow on top and in the surroundings have a change in scale as well, there is an uncertainty of the location and size of the lakes. A comparison of the lakes and their surroundings is made, and the result is shown in Figure 4.5. The differences are computed as the values of the centres subtracted by those of the buffer zones. Some of the coherence values are missing due to the noisy images during the melt season. Among the sampled lakes, Lake 2 shows a clear centre in amplitude, while Lake 3 shows it in coherence. The uncertainty of locating these lakes and determining their sizes is thus comparatively low. In combination, Lake 1 has the largest uncertainty, and in fact no optical image has proved whether it is actually a lake. On the other hand, although Lake 4 has been proven

to be a meltwater feature, it shows a lower amplitude than the surroundings for most of the time. It is likely that the central area has been taken too small, hence a 0.005-degree buffer zone essentially may still be within the centre. Therefore, a universal buffer size may not be optimal for this experiment.

Despite the uncertainty, the quantification of the temporal change in amplitude and coherence for each lake is still helpful. Lake 2 and Lake 5 are taken as examples and shown in Figure 4.6 and Figure 4.7. The ranges of the values are less referable because they are more sensitive to speckles. Given the global variation in Figure 4.1a and Figure 4.1b, and the reference areas in Figure 4.8 and Figure 4.9, it can be concluded that the amplitude of the lakes is lower than snow and higher than ice before the melting season. During the melting season they are similar. And after the melting season, snow and ice areas both show a bounce-back which is similar to the behaviour in Figure 4.1a, while the amplitude of the lakes gradually rises. It is thus inferred that this difference is caused by a subsurface process, such as a persistent melting or refreezing. The coherence of the lakes is low in general.

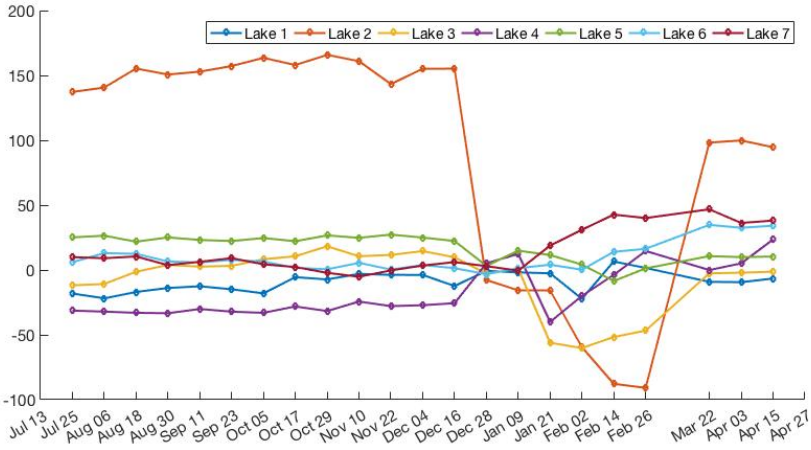


**(a)** Difference in amplitude between the lake centres and the buffer areas

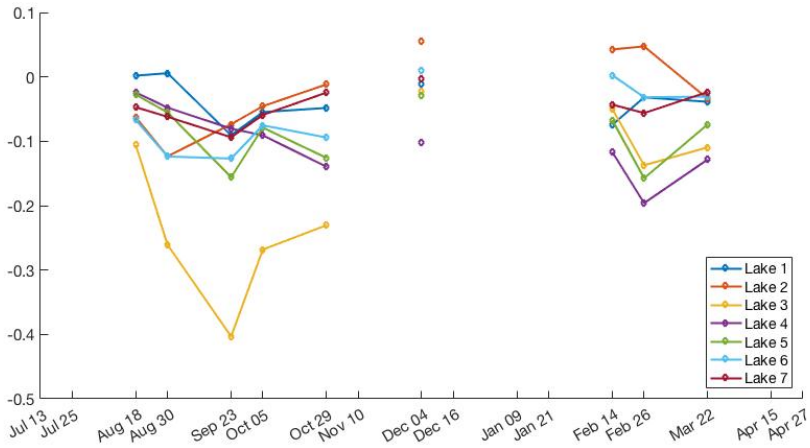


**(b)** Difference in coherence between the lake centres and the buffer areas

**Figure 4.5:** Different properties between the lake centres and the buffer areas

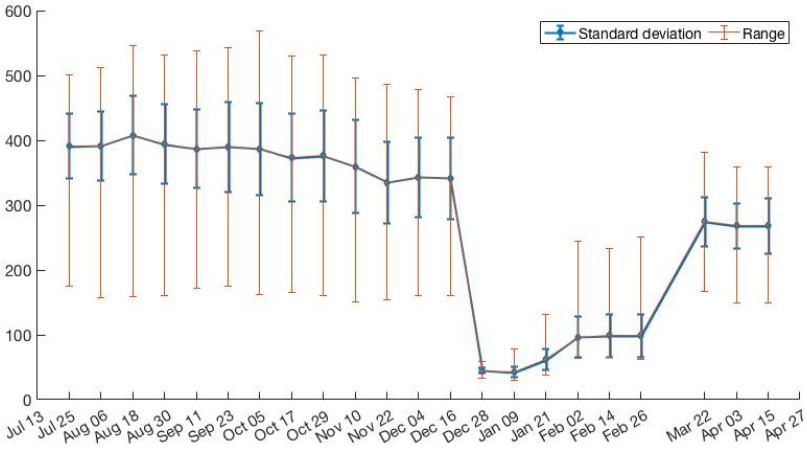


**(a)** Amplitude statistics of the centre of Lake 2

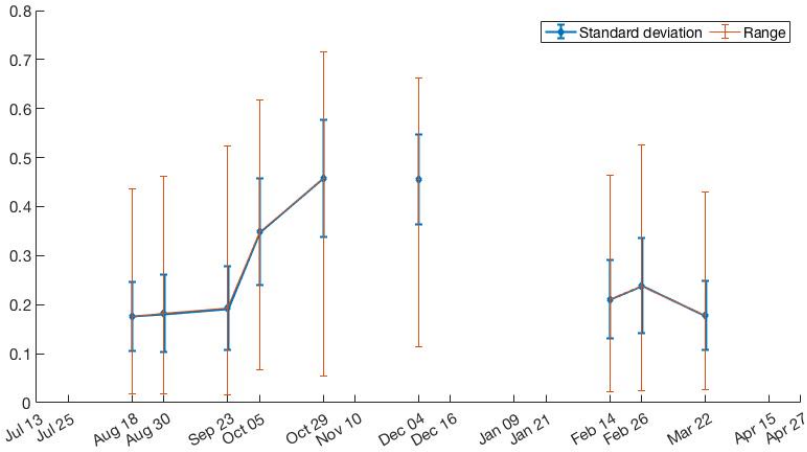


**(b)** Coherence statistics of the centre of Lake 2

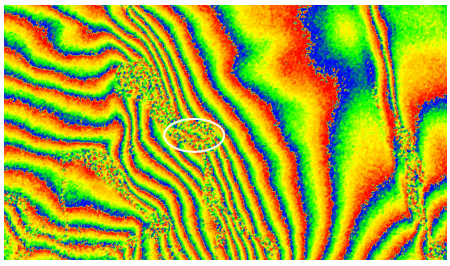

**(c)** Fringes of Lake 2 between 02/02/2018 and 14/02/2018, coherence = 0.2108

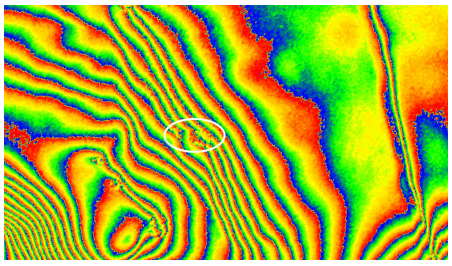

**(d)** Fringes of Lake 2 between 05/10/2017 and 17/10/2017, coherence = 0.3486

**Figure 4.6:** Statistics and fringes of the centre of Lake 2. The fringes between 05/10/2017 and 17/10/2017 can still be seen, while the other interferogram shows a noisy centre. The threshold of the coherence value for a clear fringe pattern might be between 0.21 and 0.34

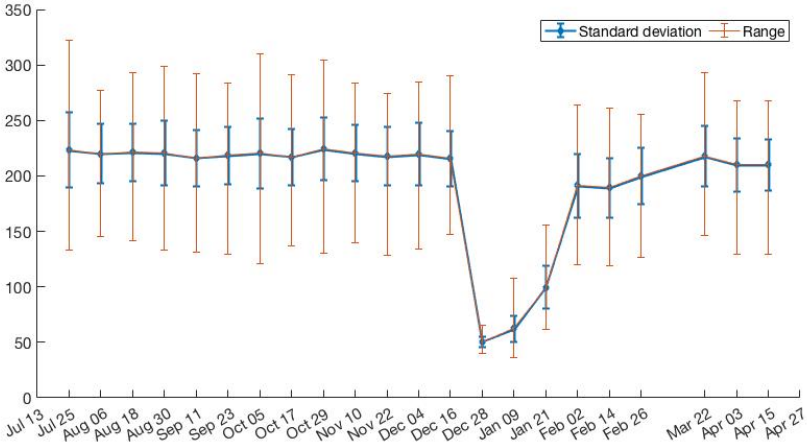


**(a)** Amplitude statistics of the centre of Lake 5

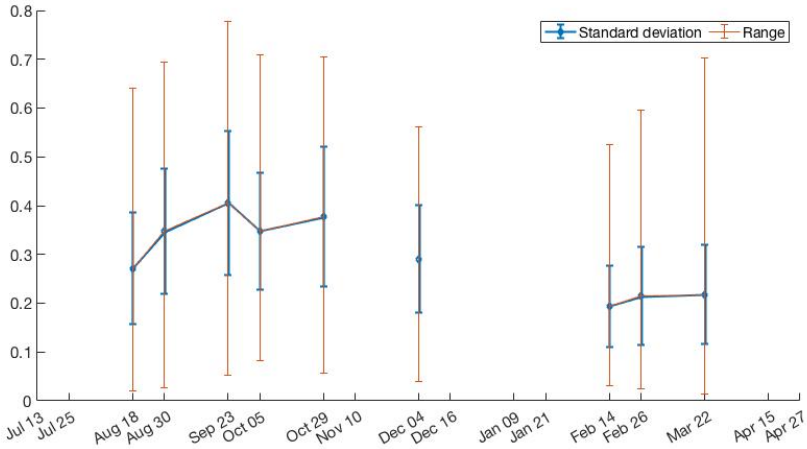


**(b)** Coherence statistics of the centre of Lake 5

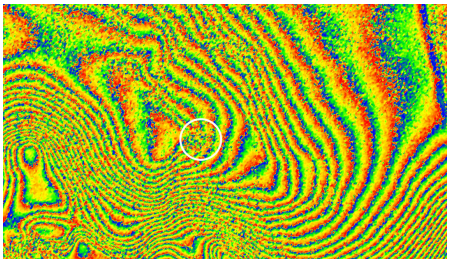

**(c)** Fringes of Lake 5 between 25/07/2017 and 06/08/2017, coherence = 0.2707

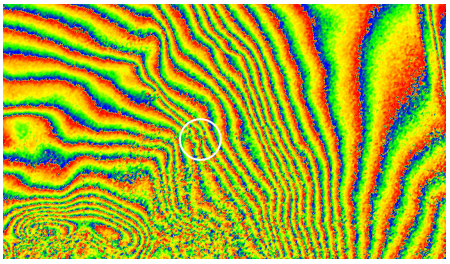

**(d)** Fringes of Lake 5 between 22/11/2017 and 04/12/2017, coherence = 0.2904

**Figure 4.7:** Statistics and fringes of the centre of Lake 5. The similar comparison of fringes as before is made. The threshold of the coherence value for a clear fringe pattern might be around 0.29

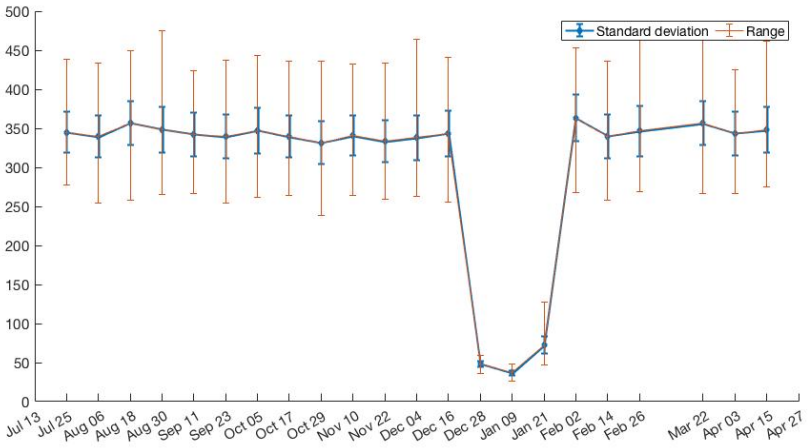


**(a)** Amplitude statistics of Reference 5

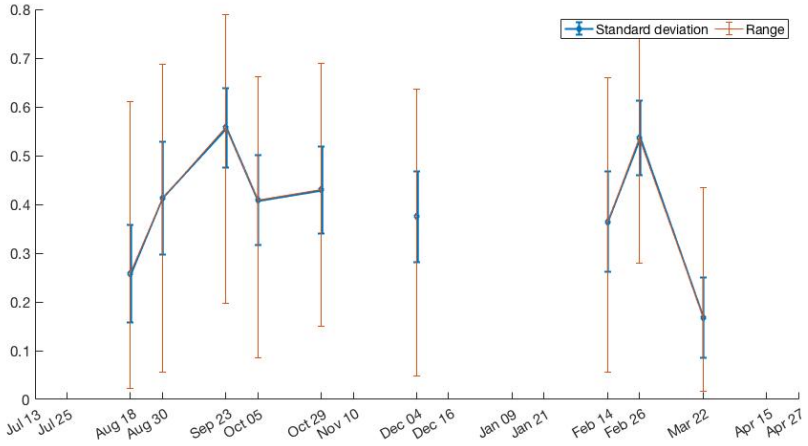


**(b)** Coherence statistics of Reference 5

**Figure 4.8:** Statistics of a typical snow sample

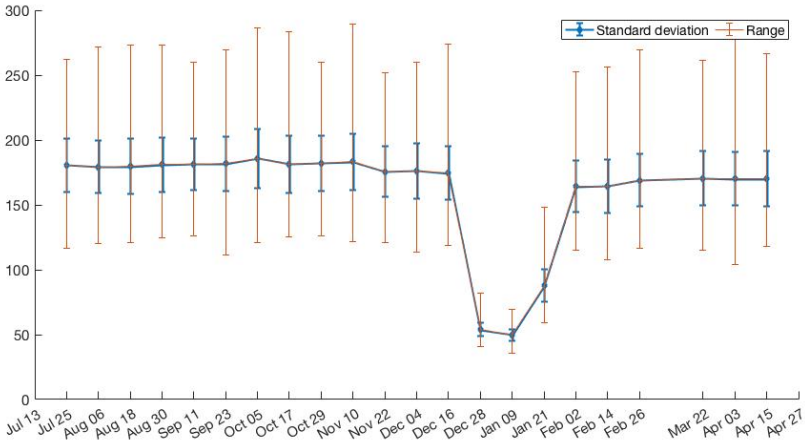


**(a)** Amplitude statistics of Reference 7

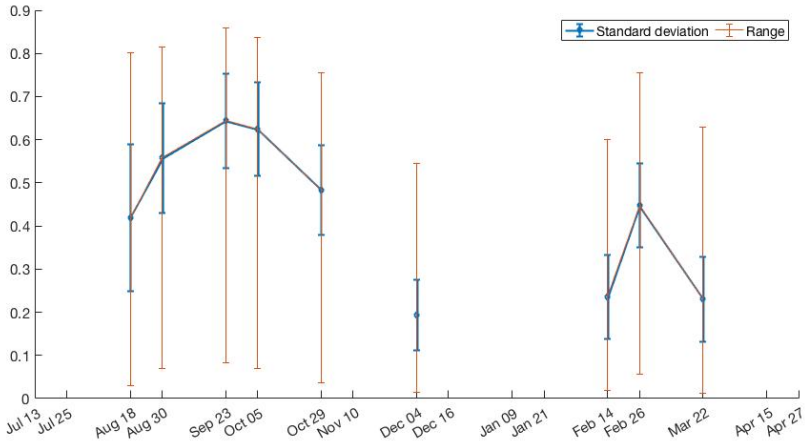


**(b)** Coherence statistics of Reference 7

**Figure 4.9:** Statistics of a typical blue ice sample

Another method to assess the scale of the lakes is to plot the amplitudes along a certain track over the lakes. The tracks are marked in Figure 4.10. The spatial assessment shows different patterns in different seasons and different topographical environments. The lake indexed as Lake 2 in Figure 4.4a is located in the wet-snow zone, where the overall amplitude is expected to be high. It has the typical amplitude feature, meaning that the centre is brighter than the outer area during the cold seasons. And the brighter area is slightly larger in winter than in spring, which means that the snow cover may be decreasing. It may be then exposed on the surface in summer, because the amplitude of the centre is lower than the surroundings. The amplitude in autumn 2018 may show a refreezing behaviour, as the centre gains some amplitude again.

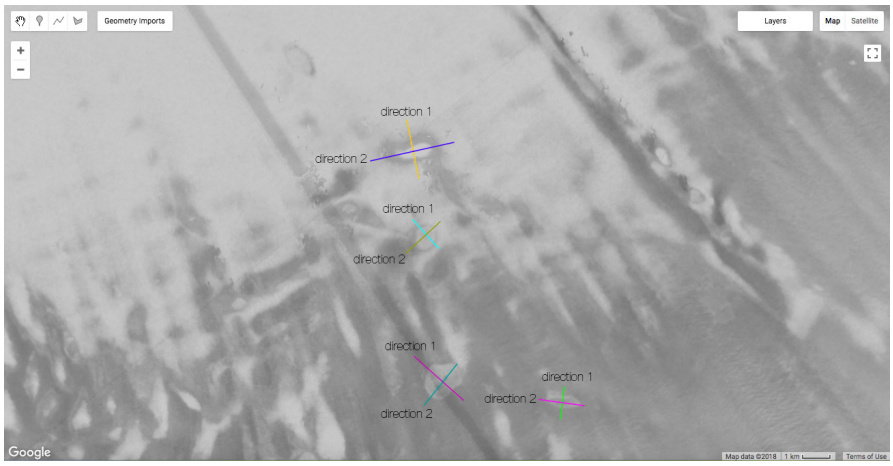


**Figure 4.10:** Delineation tracks

Lake 6 is located in the blue ice area, where the amplitude should be low. In general, the lake has a brighter amplitude than the surrounding. It shows a drop in the centre during spring and summer, which might be the result of an exposure of water.

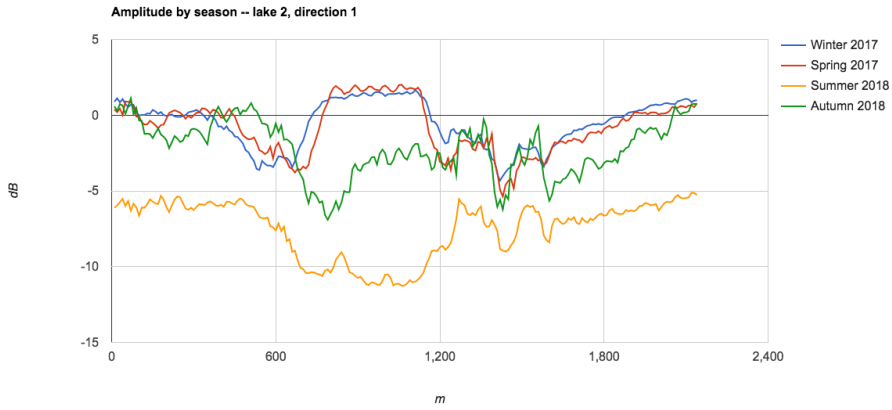


**Figure 4.11:** Delineation of Lake 2, in the direction of approximately the largest extent

The spatial and temporal assessments of the amplitude and coherence not only reveal several characteristics of the subsurface lakes such as scale change and time of intense melting, but also indicate that the meltwater may remain ponded throughout the whole study period. With this information, detection of the lakes can be

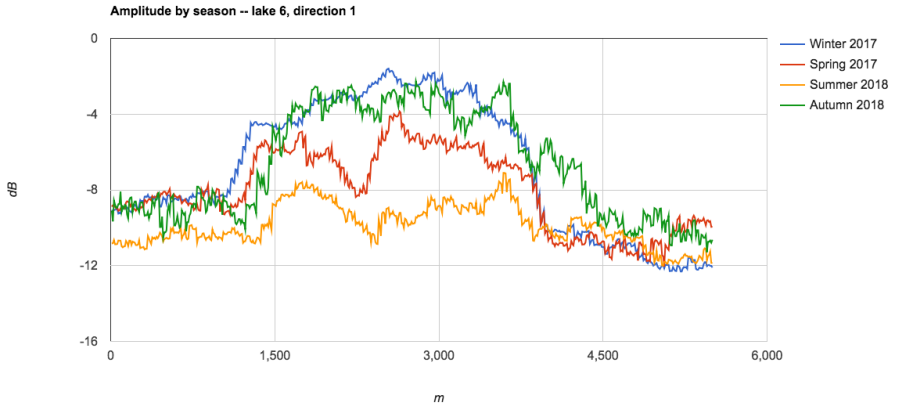


**Figure 4.12:** Delineation of Lake 6, in the direction of approximately the largest extent

carried out using the data from all the acquisition dates.

The lakes visited and mapped from the ALOS acquisition are first shown in Figure 4.13a. The background image is a cloud-free Landsat 8 image in October, 2017. This image shows that at this moment the lakes are indeed under the surface. And because the ALOS data and Landsat 8 image are from different times of different years, both annual and inter-annual differences exist. What can be expected is that in this region the lakes are covered by ice and snow for most of the time. These lakes all have the potentiality of being exposed on the surface when a strong melt happens. Then the valid amplitude and coherence georeferenced to the map are shown from Figure 4.13b to Figure 4.13f.

From the images with an overall high amplitude, it can be seen that when the lakes are hidden under the surface, the edges of the lakes tend to be darker than the surrounding, while the centre may appear brighter than the boundary because of the snow cover. And when the lakes are open, they appear completely dark. The ice and water features can both give a low coherence. This characteristic is most obvious in Figure 4.13e. These characteristics do correspond to the statistics above. However, during strong melting periods, even if the coherence is not completely low, it is hard to distinguish lakes from the surroundings (Figure 4.13f). It can be presumed from here that wet snow may also contribute to a decrease in coherence.

To summarise, the lakes show up in the georeferenced images as follows:

- When the amplitude is high in the whole area, the lakes show up with a dark boundary and a brighter centre.
- When the image has a high coherence, the lakes are darker than surroundings.
- When the area has a low amplitude, but the contrast is still obvious, the lakes appear darker than surroundings.
- When the icy parts or sastrugi share the same characteristics as described above, a morphology criterion can be applied: the boundaries of the water features are smoother than the other features.

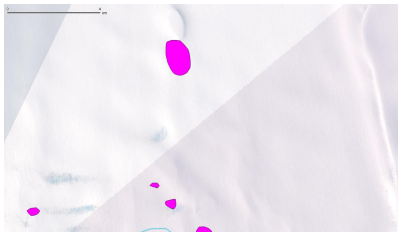

(a) Landsat 8 background

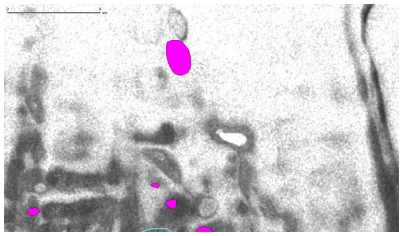

(b) Amplitude on 05/10/2017

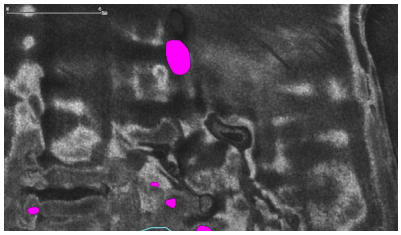

(c) Amplitude on 21/01/2018

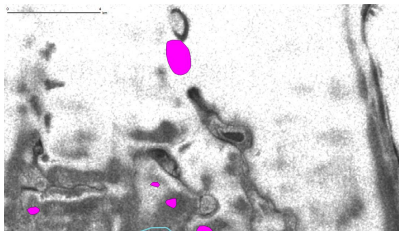

(d) Amplitude on 02/02/2018

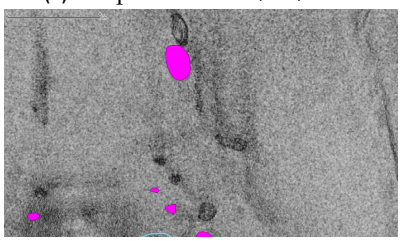

(e) Coherence between 05/10/2017 and 17/10/2017

(f) Coherence between 21/01/2018 and 02/02/2018

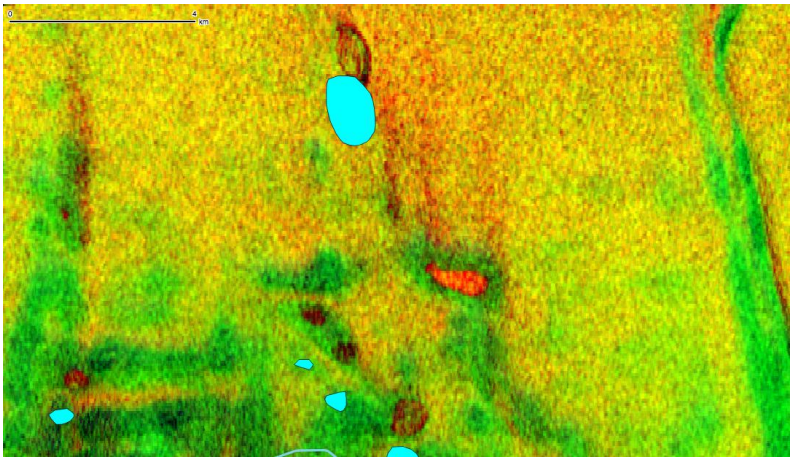

(g) False colour image; R band is Figure 4.13b, G band is Figure 4.13e and B band is Figure 4.13c

**Figure 4.13:** Lakes with different Sentinel-1 properties

The images are then combined into a false colour image. The high amplitude, high coherence and low amplitude values are scaled to unsigned 8-bit integers and assigned to R/G/B bands respectively. Based on the criteria above, the lakes are expected to show up as red/orange spots with a smooth green/black outline, as is depicted in Figure 4.13g. After detecting the lakes with the false colour images, available (semi-)cloud-free Landsat 8 images are used again for validation.

The bursts in Figure 3.2 are all processed in the same manner, and the result is shown in Figure 4.14a. Then the lakes are recognised manually as Figure 4.14b, Figure 4.14d and Figure 4.14f show.

The first comparison of the outcome is made with the ALOS mapping from Lenaerts et al. [2016a], because many of the lakes mapped in this study have been visited on site. The lakes mapped in this study are generally distributed in the same areas as has been mapped by Lenaerts et al. [2016a]. Because the previous knowledge indicates that the displacement between the two methods can be related to the ice velocity, the displacement is then computed and removed from the locations from this study. The comparison between locations is made by comparing the overlapping areas of the lakes. After removing the displacement, the comparison in the area of Figure 4.13 is visualised in Figure 4.15. The result shows a great match between the studies. For the lakes that have not been visited from the Lenaerts et al. [2016a] study, the correspondence between this study and the ALOS measurement is relatively low, while this study also mapped a certain amount of lakes that have not been mapped by Lenaerts et al. [2016a]. Because both methods are based on the authors' experience and insufficient data, misinterpretation can occur, especially given the outcome that the smaller lakes tend to differ between the two methods. The difference may also be caused by an inter-annual evolution of the lakes, as the older lakes may disappear and new lakes may form. A difference in penetration depth can also cause the difference in detection, as the lakes that are buried deeper may be hidden from the C-band radar. And with the amplitude information only, the ALOS result may miss some lakes as well.

For further validation, the Landsat 8 images from January 2018 are taken and shown in Figure 4.14c, Figure 4.14e and Figure 4.14g. In all the available images, not all the cloud cover has been properly removed. The combination of the Landsat images from October 2017 and January 2018 aims to reveal the lakes that were open or free from the snow cover (but still with blue ice on top) when the melt occurred. It can be seen from the comparison that, although all the lakes mapped in this study are indeed subsurface lakes, there is a subsurface drainage system in the middle of the ice shelf that has been missed. It is likely that the drainage system only forms in the melting period, or they have a different characteristic than the lakes. It can also be caused by a combination of both. All the streams show up as dark features in amplitude images, and bright features in coherence images. This characteristic has not been observed in the lakes that have been visited. In addition, twenty-two lakes have also been missed likely due to the same reason. Figure A.2 gives the average coherence over the time series, and it can be seen that the water and blue ice features are dark indeed, whilst the drainage system has a high coherence.

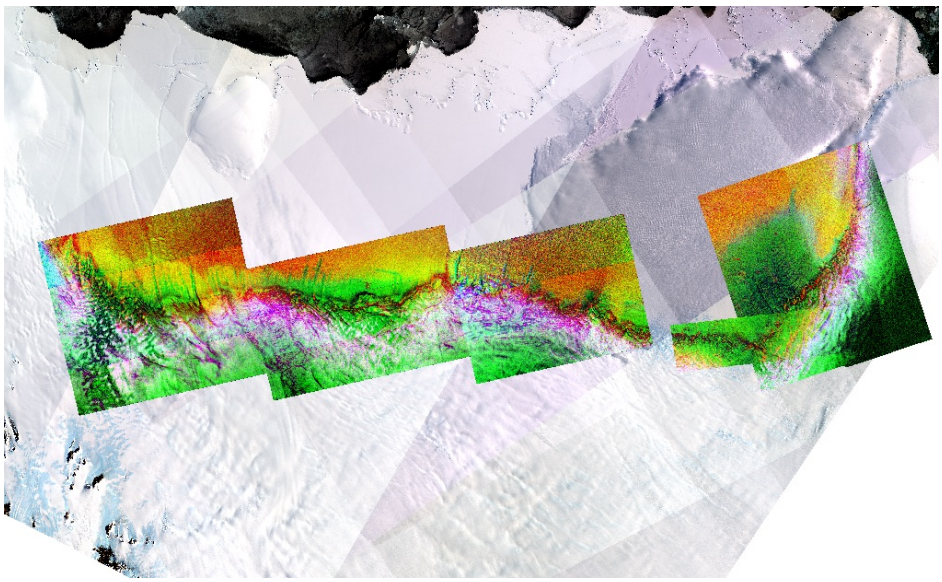

(a) False colour image of all inspected bursts

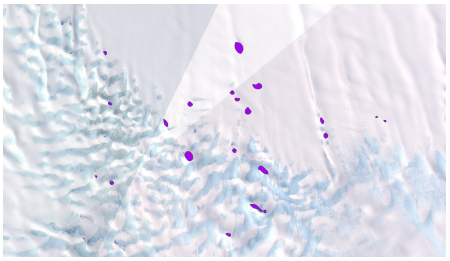

(b)

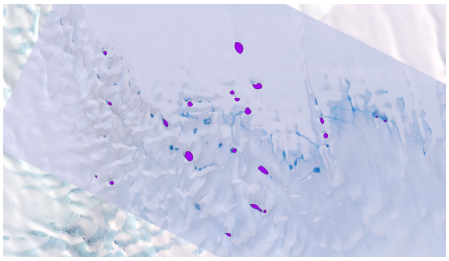

(c)

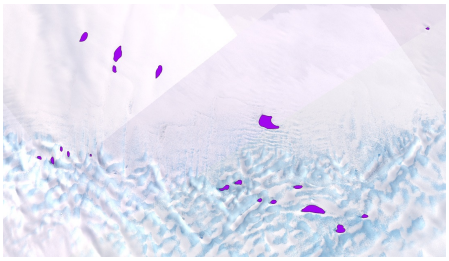

(d)

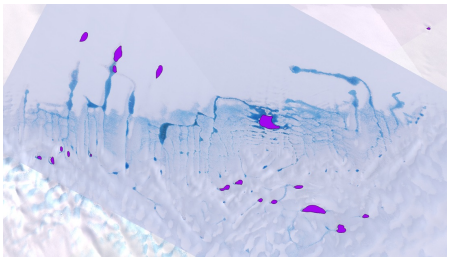

(e)

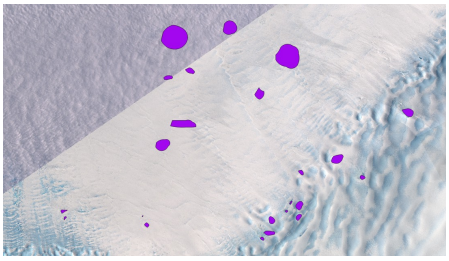

(f)

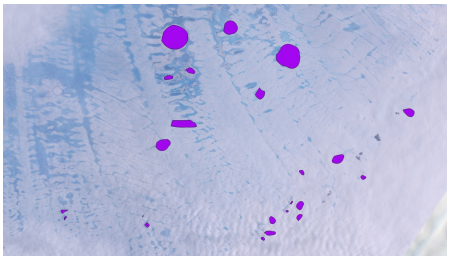

(g)

**Figure 4.14:** Subsurface lakes mapped and validated by this study

In conclusion, it can be learned from this static study that the lakes detected by InSAR can match the ground truth in general. This method is also restricted in the following aspects:

- It is mostly applicable when slight or no melt occurs, as the melt tends to lead to a noisy image both in amplitude and coherence.
- The 12-day revisit time may result in a large incoherence and a lack of data.

Hence, a dynamic analysis should be carried out in the complete time period. An additional conclusion is that the lakes that can be detected by this static study tend to be preserved in winter.

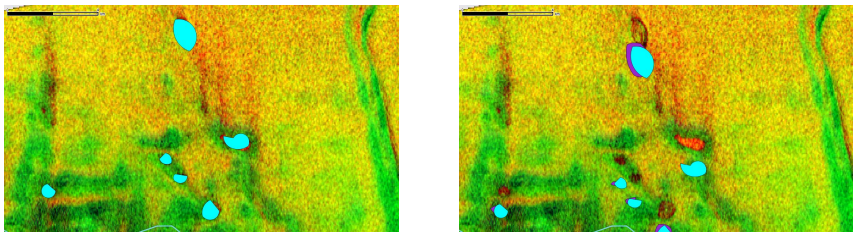

**(a)** Lakes mapped by this study **(b)** Removal of ice velocity

**Figure 4.15:** Result of this study (in cyan) and comparison with the study of Lenaerts et al. [2016a] (in purple) after removal of ice velocity

## 4.3 DYNAMIC BEHAVIOURS

### Melting and refreezing

The channels in the middle of the ice shelf, as is mentioned in the previous section, showed different characteristics and are therefore not detectable in the same manner. Because the channels generally have a high coherence, this section seeks the possibility to observe the water features from interferograms.

The optical images of the channels are provided by Figure 4.14d and Figure 4.14e. These images show a rapid increase in the exposure of the channels between October 2017 and January 2018. The 'lakes' detected in these images are more likely to be snow- and ice-covered parts of the channels. Given the shapes and size of these channels, it is less informative to carry out the same assessments as those of the lakes. But the evolution is obvious enough from the overall interferograms. Figure 4.16a and Figure 4.16b show an increased ice cover of the channels, which refers to a gradual refreeze process. The behaviours can be better reflected by the corresponding interferograms. In Figure 4.16g, the fringes are dominated by ice velocity, and are continuous in the channel areas. In Figure 4.16h, the interferogram is corrupted due to the intense surface melting. The channels can then be seen from Figure 4.16i as interruptions between the fringes. It can be seen that some fringes are preserved in between, as a result of the solid ice and snow covers. The fringes finally get more connected again in Figure 4.16j, when the surface becomes more solid. They are however not completely solid because the refreeze is incomplete.

(a) Landsat image in January 2018

(b) Landsat image in March 2018

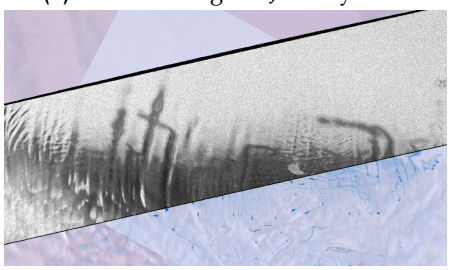

(c) Amplitude on 05/10/2017

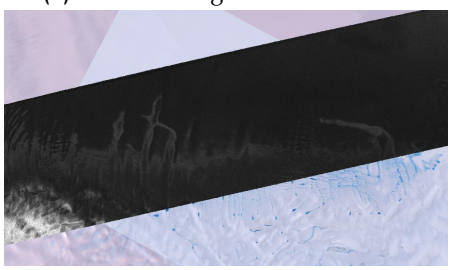

(d) Amplitude on 28/12/2017

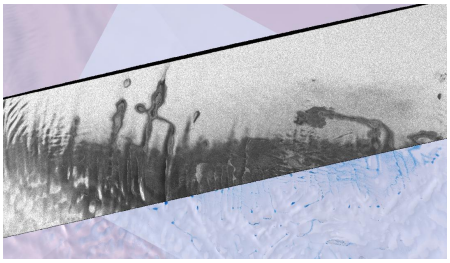

(e) Amplitude on 14/02/2017

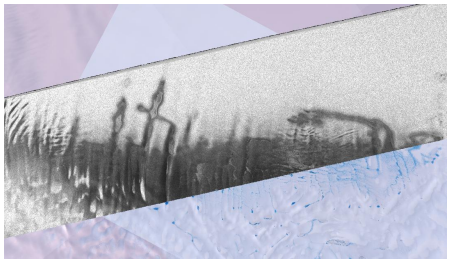

(f) Amplitude on 03/04/2017

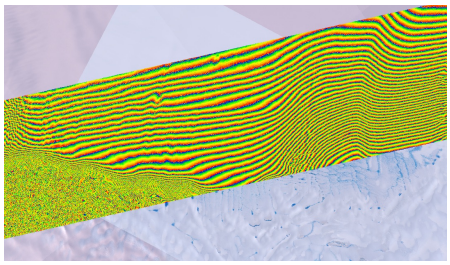

(g) Interferogram between 05/10/2017 and 17/10/2017

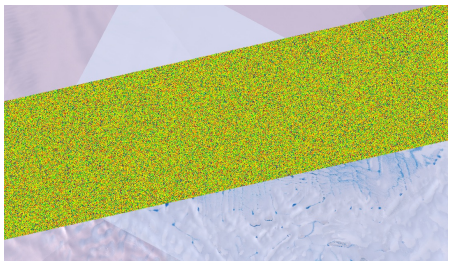

(h) Interferogram between 28/12/2017 and 09/01/2018

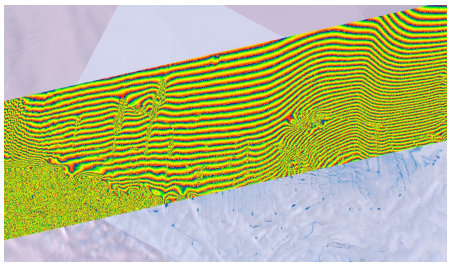

(i) Interferogram between 14/02/2018 and 26/02/2018

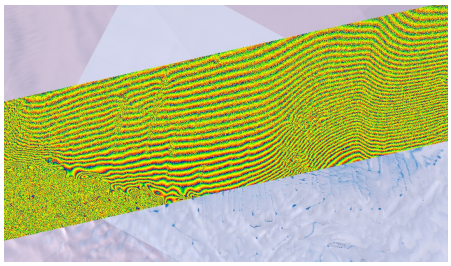

(j) Interferogram between 22/03/2018 and 03/04/2018

**Figure 4.16:** Subsurface channels and their evolution

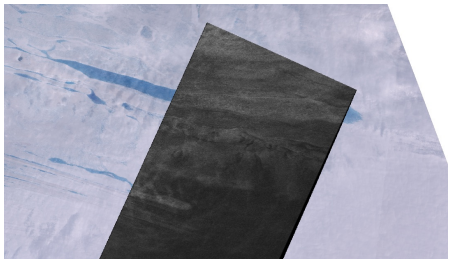

**(a)** Amplitude on 04/01/2017

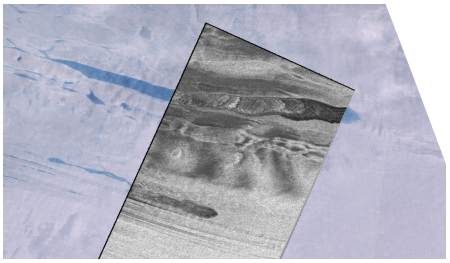

**(b)** Amplitude on 28/01/2017

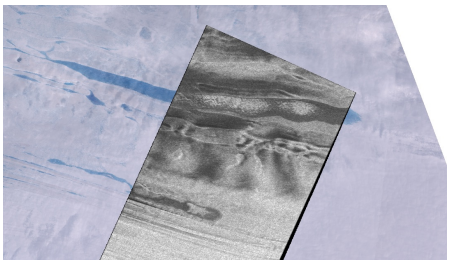

**(c)** Amplitude on 29/03/2017

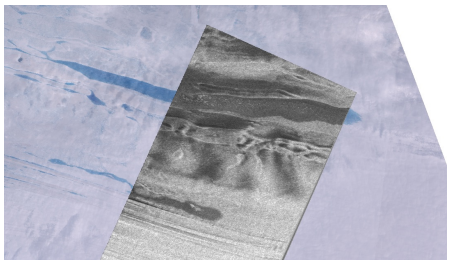

**(d)** Amplitude on 22/04/2017

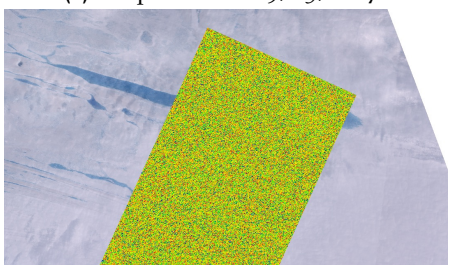

**(e)** Interferogram between 04/01/2017 and 16/01/2017

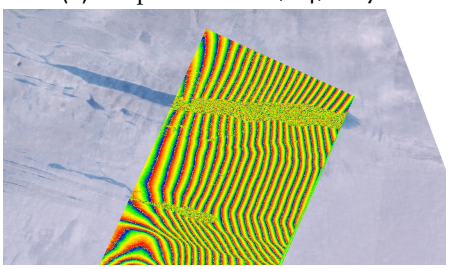

**(f)** Interferogram between 22/01/2017 and 28/01/2017

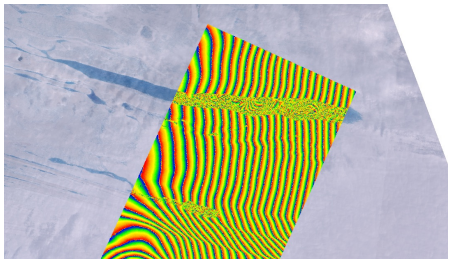

**(g)** Interferogram between 09/02/2017 and 15/02/2017

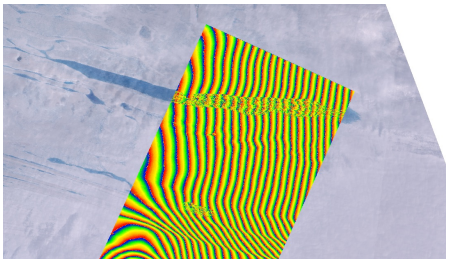

**(h)** Interferogram between 11/03/2017 and 17/03/2017

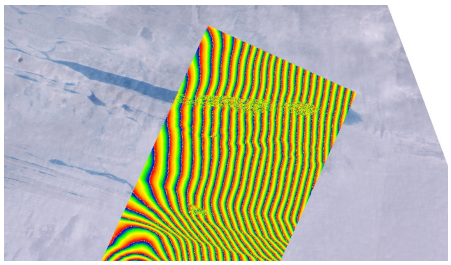

**(i)** Interferogram between 29/03/2017 and 04/04/2017

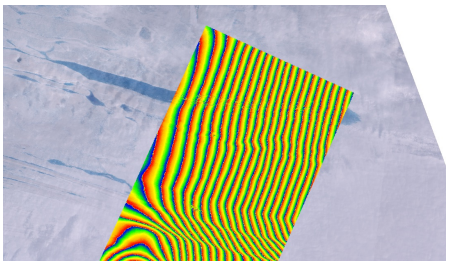

**(j)** Interferogram between 22/04/2017 and 28/04/2017

**Figure 4.17:** Subsurface channel and the evolution over Amery

This behaviour is detected more completely over the Amery Ice Shelf, because the event happened in 2017, and the data were acquired with a 6-day revisit time except for the ones in Figure 4.17e. The refreeze process is depicted by Figure 4.17. In Figure 4.17g, there are fringes in the middle of the channel, but they are disconnected. This may be a result of floating ice. Figure 4.17h shows the fringes starting to get connected, yet still noisy as a result of the dynamic process. The fringes gradually get smooth and connected to the environment.

Since neither of the channel areas has been visited, and the Landsat images lack the availability to show whether the channels only appeared during the melt seasons and really froze through afterwards. The conclusion drawn from the fringe patterns is not definite. It is only based on the knowledge inferred from Hirose et al. [2008] and Antonova et al. [2016]. Although the regions of interest of this study differ from the Arctic, the results may have a certain correspondence. For the channels in the middle of the RBIS, the time series of the amplitudes is less representative due to the data availability. The channel on Amery Ice Shelf shows the evolution from the amplitude perspective as well. During the strong melting in early January, the whole area loses amplitude and coherence, but if the water surface is open, it is likely to be rough because of the blowing wind, resulting a relatively high amplitude in comparison to the surroundings. The gradual freezing-up can be seen from the increasing amplitude, and as the ice gets more grounded, the bright area shrinks due to the dielectric difference of the interface between the new ice and old ice. The grounded ice finally gives a low amplitude.

### Collapsing and filling

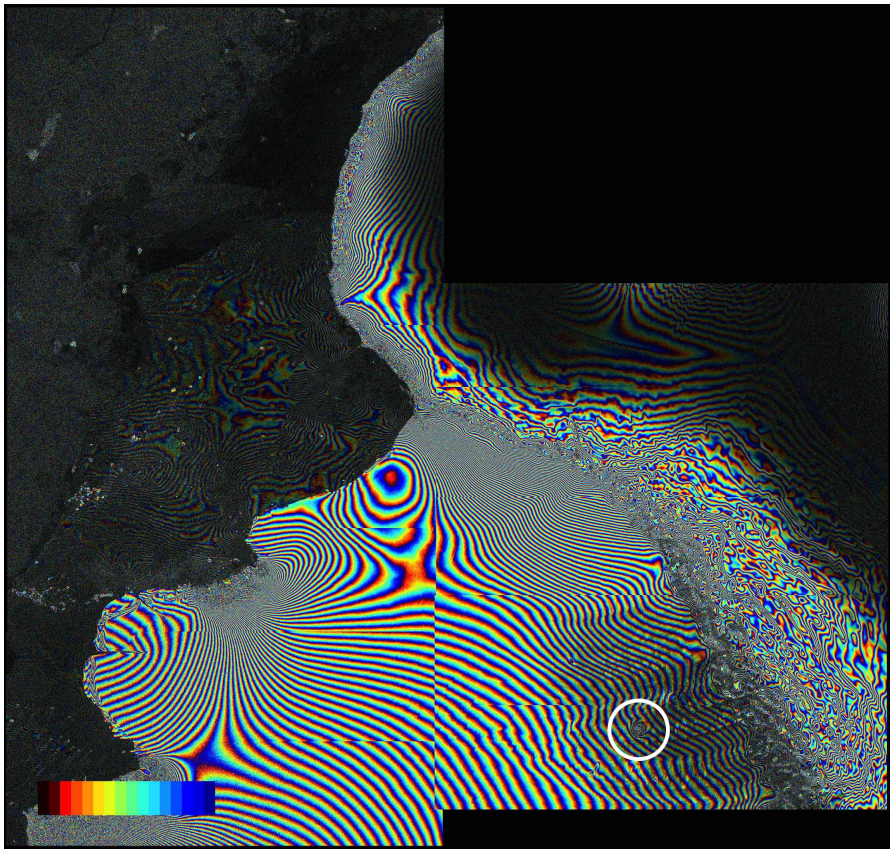

**Figure 4.18:** Interferogram with phase anomaly

Figure 4.18 is the interferogram obtained over the eastern part of the ice shelf between Dec. 4, 2017 and Dec. 16, 2017 (the latter as the master image), similar region to Figure 2.7. Comparing the two images, there are several distinct anomalies in the image taken in 2017, the most obvious one corresponding to burst No. 5, swath No. 2 of descending track No. 136 in Figure 3.2 and marked with a circle. This burst is then zoomed in and further observed (Figure 4.20), and it is verified that the largest anomaly is only temporary. This observation eliminates the possibility that the topography causes this phenomenon, therefore it is likely that a surface or subsurface behaviour exists.

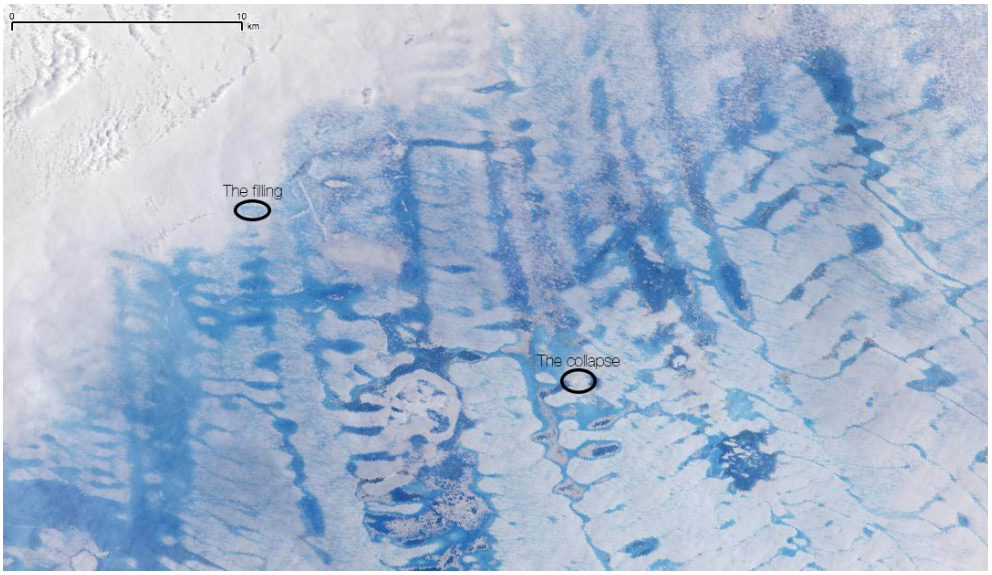


**Figure 4.19:** Landsat 8 image on 11/01/2018, with the anomalies

The large fringe anomaly not only differs from the surroundings in density, but also in the orientation of cycles. The surroundings change in range direction as red-yellow-green-blue while the anomaly goes inversely. Because it is known that the ice velocity in this area is dominant and moving away from the satellite (towards the ocean), the anomaly moves towards the satellite which should be an uplift. Since it has been previously mapped as a lake, this can be inferred as a temporal lake evolution. Corresponding Landsat 8 images have been shown in Figure 2.3 as a validation for this outcome. The images in combination indicate that this lake has experienced a collapse, which causes an elevation change, with corresponding elevation changes in the surroundings due to the conservation of mass. One of the neighbouring lakes that shows a subsidence may has experienced a filling event, as the gravity adds load to the ice layer [Banwell et al., 2013].

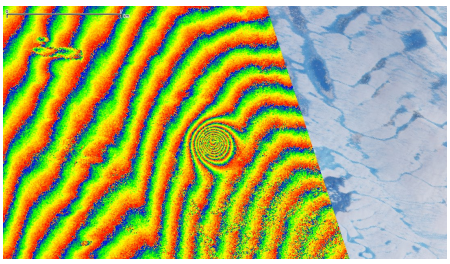

**(a)** Interferogram between 04/12/2017 and 16/12/2017

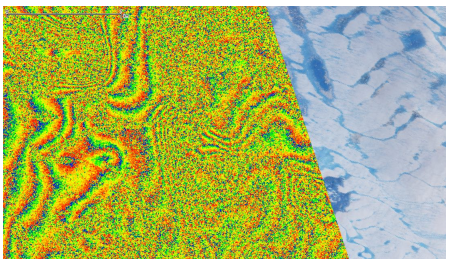

**(b)** Interferogram between 21/01/2018 and 02/02/2018

**Figure 4.20:** Observation of phase anomalies, corresponding to the collapse in Figure 4.19

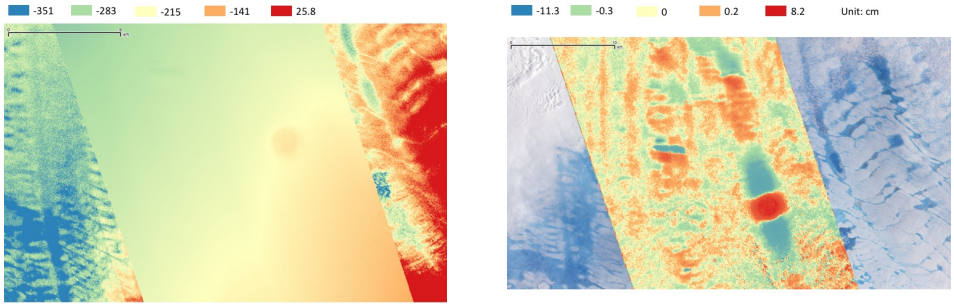


**(a)** Unwrapped phase **(b)** Detrended result

**Figure 4.21:** Detrending over the region

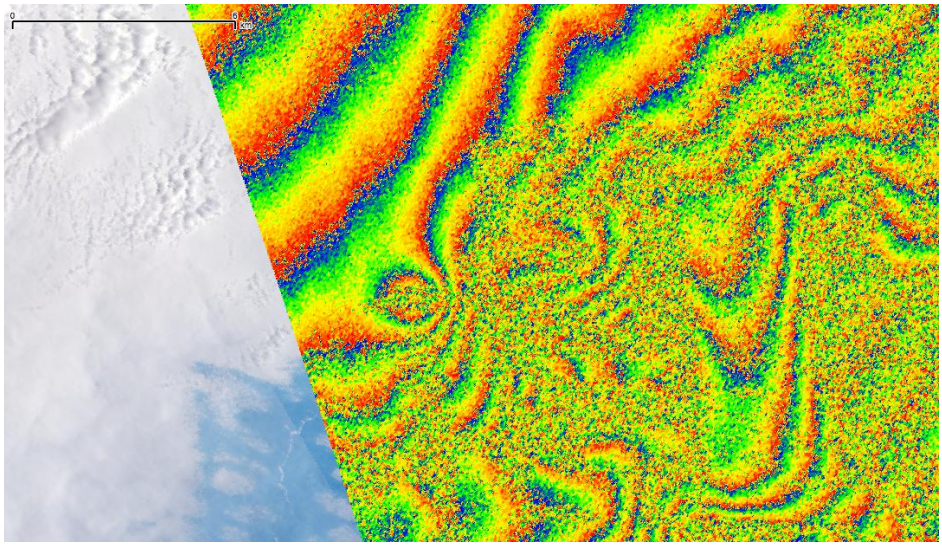

**(a)** Interferogram between 02/02/2018 and 14/02/2018

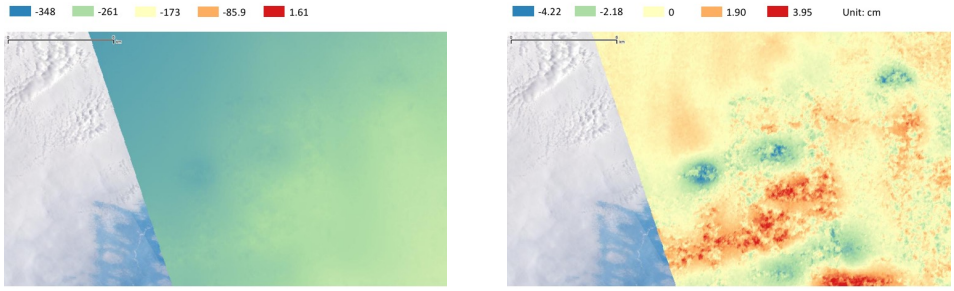


**(b)** Unwrapped phase **(c)** Detrended result

**Figure 4.22:** Phase anomaly and detrending over the region, corresponding to the filling in Figure 4.19

It is then expected that such method can be used for other regions, but during the period of the data acquisition, no such clear fringe patterns has been captured in the western and central parts over the RBIS. In the same region, only a gradual subsidence has been detected (Figure 4.22). This might be the result of the filling of the lake. The increased mass of water contributes to the local pressure, hence a subsidence occurs [Banwell et al., 2013]. Therefore, it can be concluded that the InSAR method is possible to detect the various dynamic behaviours of the lakes, but has the limitation that the fringe anomaly should be obvious. This requires the coherence to be generally high, not only because it guarantees that the fringe pattern can be observed by experts, but also because the unwrapping is more reliable when the interferogram has a high quality. And because there is no perfect detrending method to completely remove the movement of the surroundings from the local movement, when the distinction between the movement of the lake and that of the surroundings is small, it may miss detecting the local event. For example, although Lenaerts et al. [2016a] have surveyed that a lake on the western side of the ice shelf did experience a collapse, no interferogram is capable of capturing this event.

# 5 CONCLUSIONS AND FUTURE WORK

In this study, the possibility to use InSAR technique to detect subsurface meltwater has been discussed. The performance is generally promising.

It can be learned that the C-band radar can indeed penetrate a certain depth within the ice- and snow-covered area. And compared to the ALOS image, the InSAR method may have a smaller spatial coverage, but can detect the subsurface meltwater features to the same extent. Moreover, the InSAR method is capable of the detection of dynamic behaviours of these features.

From the static and dynamic detection, it can be concluded that although they involve the validation with the available optical imagery, the outcome corresponds to the validation. Therefore, by using a combination of the amplitude and coherence information of InSAR, little or no reference of the optical imagery is needed. This breaks the limitation of data during cloudy and dark times. And the static and dynamic behaviours are as follows:

- The lakes do appear in the same region as has been studied by Lenaerts et al. [2016a]. And the lack of coherence during winter time may indicate that the water features are not completely frozen. The meltwater features have a variation in scale and experience a certain displacement over time. The scale variation provided by this study is mainly measured by amplitude information, and may be due to the melting and forming of a frozen layer on top, or a change of the snow/ice property such as density and particle size.
- Some channels behave differently from the lakes, which may be caused by a different local topography hence different local climate. Although not validated by *in situ* study, it has been inferred that the channels are more dynamic and possibly frozen through. The detection of this behaviour can be achieved with a combination of the amplitude and interferograms.
- The instant behaviours such as lake collapse and filling can be captured given a certain coherence. From this study, this coherence value is approximately 0.29, which is not completely dependent on the local temperature. Therefore, the completeness of the interferogram is essential in this aspect.

However, there remains some space for improvement:

- The interpretation of the InSAR results needs to be explored more thoroughly.
- As can be seen from Figure C.1, the incoherent cross-correlation method can improve the coregistration to some extent, provided that the noise is efficiently reduced; but the noise reduction is not yet covered by this study.
- The classification is purely based on the experience of the author, therefore it is more reliable to manually recognise the lakes; for a larger scale, an automatic and reliable method should be proposed.

# BIBLIOGRAPHY


Adodo, F. I., Remy, F., and Picard, G. (2017). Seasonal variations of the backscattering coefficient measured by radar altimeters over the antarctica ice sheet. *The Cryosphere Discussions*, pages 1–15.

Antonova, S., Duguay, C., Kääb, A., Heim, B., Langer, M., Westermann, S., and Boike, J. (2016). Monitoring Bedfast Ice and Ice Phenology in Lakes of the Lena River Delta Using TerraSAR-X Backscatter and Coherence Time Series. *Remote Sensing*, 8(11):903.

Banda, F., Dall, J., Tebaldini, S., and Rocca, F. (2013). Tomographic SAR analysis of subsurface ice structure in Greenland: First results. In *2013 IEEE International Geoscience and Remote Sensing Symposium - IGARSS*. IEEE.

Banwell, A. F., MacAyeal, D. R., and Sergienko, O. V. (2013). Breakup of the Larsen B Ice Shelf triggered by chain reaction drainage of supraglacial lakes. *Geophysical Research Letters*, 40(22):5872–5876.

Barla, G., Tamburini, A., Del Conte, S., and Giannico, C. (2016). InSAR monitoring of tunnel induced ground movements. *Geomechanics and Tunnelling*, 9(1):15–22.

Beckmann, P. and Spizzichino, A. (1987). *The scattering of electromagnetic waves from rough surfaces*. Artech House Radar Library.

Bindschadler, R., Choi, H., Wichlacz, A., Bingham, R., Bohlander, J., Brunt, K., Corr, H., Drews, R., Fricker, H., Hall, M., Hindmarsh, R., Kohler, J., Padman, L., Rack, W., Rotschky, G., Urbini, S., Vornberger, P., and Young, N. (2011). Getting around Antarctica: new high-resolution mappings of the grounded and freely-floating boundaries of the Antarctic ice sheet created for the International Polar Year. *The Cryosphere*, 5(3):569–588.

Chu, V. W. (2013). Greenland ice sheet hydrology. *Progress in Physical Geography*, 38(1):19–54.

Church, J. A., White, N. J., Konikow, L. F., Domingues, C. M., Cogley, J. G., Rignot, E., Gregory, J. M., van den Broeke, M. R., Monaghan, A. J., and Velicogna, I. (2011). Revisiting the Earth's sea-level and energy budgets from 1961 to 2008. *Geophysical Research Letters*, 38(18):n/a–n/a.

Copernicus (2017). Open Access Hub. https://scihub.copernicus.eu. Accessed 2 Nov. 2017.

De Zan, F. (2011). Coherent Shift Estimation for Stacks of SAR Images. *IEEE Geoscience and Remote Sensing Letters*, 8(6):1095–1099.

De Zan, F. (2014). Accuracy of Incoherent Speckle Tracking for Circular Gaussian Signals. *IEEE Geoscience and Remote Sensing Letters*, 11(1):264–267.

De Zan, F. and Monti Guarnieri, A. (2006). TOPSAR: Terrain Observation by Progressive Scans. *IEEE Transactions on Geoscience and Remote Sensing*, 44(9):2352–2360.

De Zan, F., Prats-Iraola, P., Scheiber, R., and Rucci, A. (2014). Interferometry with tops: coregistration and azimuth shifts. In *Proc. 10th EUSAR*.

De Zan, F., Zonno, M., and Lopez-Dekker, P. (2015). Phase Inconsistencies and Multiple Scattering in SAR Interferometry. *IEEE Transactions on Geoscience and Remote Sensing*, 53(12):6608–6616.

Dee, D. P., Uppala, S. M., Simmons, A. J., Berrisford, P., Poli, P., Kobayashi, S., Andrae, U., Balmaseda, M. A., Balsamo, G., Bauer, P., Bechtold, P., Beljaars, A. C. M., van de Berg, L., Bidlot, J., Bormann, N., Delsol, C., Dragani, R., Fuentes, M., Geer, A. J., Haimberger, L., Healy, S. B., Hersbach, H., Hólm, E. V., Isaksen, L., Kållberg, P., Köhler, M., Matricardi, M., McNally, A. P., Monge-Sanz, B. M., Morcrette, J.-J., Park, B.-K., Peubey, C., de Rosnay, P., Tavolato, C., Thépaut, J.-N., and Vitart, F. (2011). The ERA-Interim reanalysis: configuration and performance of the data assimilation system. *Quarterly Journal of the Royal Meteorological Society*, 137(656):553–597.

Delft Institute of Earth Observation and Space Systems (DEOS) (2008). *Delft Object-oriented Radar Interferometric Software User's manual and technical documentation*. Delft University of Technology, v4.02 edition.

Dupont, T. K. and Alley, R. B. (2005). Assessment of the importance of ice-shelf buttressing to ice-sheet flow. *Geophysical Research Letters*, 32(4):n/a–n/a.

ESA (2018a). Instrument Payload. https://sentinel.esa.int/web/sentinel/missions/sentinel-1/instrument-payload. Accessed 13 Feb. 2018.

ESA (2018b). Products and Algorithms. https://sentinels.copernicus.eu/web/sentinel/technical-guides/sentinel-1-sar/products-algorithms. Accessed 1 Nov. 2017.

Fretwell, P., Pritchard, H. D., Vaughan, D. G., Bamber, J. L., Barrand, N. E., Bell, R., Bianchi, C., Bingham, R. G., Blankenship, D. D., Casassa, G., Catania, G., Callens, D., Conway, H., Cook, A. J., Corr, H. F. J., Damaske, D., Damm, V., Ferraccioli, F., Forsberg, R., Fujita, S., Gim, Y., Gogineni, P., Griggs, J. A., Hindmarsh, R. C. A., Holmlund, P., Holt, J. W., Jacobel, R. W., Jenkins, A., Jokat, W., Jordan, T., King, E. C., Kohler, J., Krabill, W., Riger-Kusk, M., Langley, K. A., Leitchenkov, G., Leuschen, C., Luyendyk, B. P., Matsuoka, K., Mouginot, J., Nitsche, F. O., Nogi, Y., Nost, O. A., Popov, S. V., Rignot, E., Rippin, D. M., Rivera, A., Roberts, J., Ross, N., Siegert, M. J., Smith, A. M., Steinhage, D., Studinger, M., Sun, B., Tinto, B. K., Welch, B. C., Wilson, D., Young, D. A., Xiangbin, C., and Zirizzotti, A. (2013). Bedmap2: improved ice bed, surface and thickness datasets for Antarctica. *The Cryosphere*, 7(1):375–393.

Hirose, T., Kapfer, M., Bennett, J., Cott, P., Manson, G., and Solomon, S. (2008). Bottomfast Ice Mapping and the Measurement of Ice Thickness on Tundra Lakes Using C-Band Synthetic Aperture Radar Remote Sensing. *JAWRA Journal of the American Water Resources Association*, 44(2):285–292.

Hogg, A. E. and Hilmar Gudmundsson, G. (2017). Impacts of the Larsen-C Ice Shelf calving event. *Nature Climate Change*, 7(8):540–542.

Hubbard, B., Luckman, A., Ashmore, D. W., Bevan, S., Kulessa, B., Kuipers Munneke, P., Philippe, M., Jansen, D., Booth, A., Sevestre, H., Tison, J.-L., O'Leary, M., and Rutt, I. (2016). Massive subsurface ice formed by refreezing of ice-shelf melt ponds. *Nature Communications*, 7:11897.

Hudson, S. R. and Brandt, R. E. (2005). A Look at the Surface-Based Temperature Inversion on the Antarctic Plateau. *Journal of Climate*, 18(11):1673–1696.

Johansson, A. M. and Brown, I. A. (2012). Observations of supra-glacial lakes in west Greenland using winter wide swath Synthetic Aperture Radar. *Remote Sensing Letters*, 3(6):531–539.

Kingslake, J., Ely, J. C., Das, I., and Bell, R. E. (2017). Widespread movement of meltwater onto and across antarctic ice shelves. *Nature*, 544(7650):349–352.

Koenig, L. S., Lampkin, D. J., Montgomery, L. N., Hamilton, S. L., Turrin, J. B., Joseph, C. A., Moutsafa, S. E., Panzer, B., Casey, K. A., Paden, J. D., Leuschen, C., and Gogineni, P. (2015). Wintertime storage of water in buried supraglacial lakes across the Greenland ice sheet. *The Cryosphere*, 9(4):1333–1342.

Kunz, L. and Long, D. (2006). Melt Detection in Antarctic Ice Shelves Using Scatterometers and Microwave Radiometers. *IEEE Transactions on Geoscience and Remote Sensing*, 44(9):2461–2469.

Langley, E. S., Leeson, A. A., Stokes, C. R., and Jamieson, S. S. R. (2016). Seasonal evolution of supraglacial lakes on an East Antarctic outlet glacier. *Geophysical Research Letters*, 43(16):8563–8571.

Lenaerts, J. T. M., Lhermitte, S., Drews, R., Ligtenberg, S. R. M., Berger, S., Helm, V., Smeets, C. J. P. P., van den Broeke, M. R., van de Berg, W. J., van Meijgaard, E., Eijkelboom, M., Eisen, O., and Pattyn, F. (2016a). Meltwater produced by wind–albedo interaction stored in an East Antarctic ice shelf. *Nature Climate Change*, 7(1):58–62.

Lenaerts, J. T. M., Lhermitte, S., Drews, R., Ligtenberg, S. R. M., Berger, S., Helm, V., Smeets, P., Van Den Broeke, M. R., Van De Berg, W. J., Van Meijgaard, E., Eijkelboom, M., Eisen, O., and Pattyn, F. (2016b). TanDEM-X elevation model of Roi Baudoin ice shelf, link to GeoTIFF, supplement to: Lenaerts, JTM et al. (2016): Meltwater produced by wind-albedo interaction stored in an East Antarctic ice shelf. Nature Climate Change.

Lhermitte, S. (2017). Meltwater lakes in East Antarctica. http://www.benemelt.eu/. Accessed 21 May 2018.

Ligtenberg, S. (2014). *The present and future state of the Antarctic firn layer*. PhD thesis, Utrecht University.

Luckman, A., Elvidge, A., Jansen, D., Kulessa, B., Kuipers Munneke, P., King, J., and Barrand, N. E. (2014). Surface melt and ponding on Larsen C Ice Shelf and the impact of föhn winds. *Antarctic Science*, 26(06):625–635.

Luzi, G. (2010). Ground based SAR interferometry: a novel tool for geoscience. In *Geoscience and Remote Sensing New Achievements*. InTech.

MacAyeal, D. R. and Sergienko, O. V. (2013). The flexural dynamics of melting ice shelves. *Annals of Glaciology*, 54(63):1–10.

Meehl, G. A., Stocker, T. F., Collins, W. D., Friedlingstein, P., Gaye, A. T., Gregory, J. M., Kitoh, A., Knutti, R., Murphy, J. M., Noda, A., Raper, S. C., Watterson, I. G., Weaver, A. J., and Zhao, Z.-C. (2007). *Climate Change 2007: The Physical Science Basis. Contribution of Working Group I to the Fourth Assessment Report of the Intergovernmental Panel on Climate Change*, chapter Global Climate Projections, page 747–845. Cambridge University Press, Cambridge, United Kingdom and New York, NY, USA.

Miles, K. E., Willis, I. C., Benedek, C. L., Williamson, A. G., and Tedesco, M. (2017). Toward Monitoring Surface and Subsurface Lakes on the Greenland Ice Sheet Using Sentinel-1 SAR and Landsat-8 OLI Imagery. *Frontiers in Earth Science*, 5.

Miranda, N. (2015). Definition of the TOPS SLC deramping function for products generated by the S-1 IPF. Technical report, European Space Agency.

Mooney, C. (2016). This stunning Antarctic lake is buried in ice. And that could be bad news. https://www.washingtonpost.com/news/energy-environment/wp/2016/12/12/this-dazzling-antarctic-lake-is-buried-in-floating-ice-and-that-has-scientists-worried/?utm_term=.0bd71bf49a1f. Accessed 10 Feb. 2018.

Mouginot, J., Scheuchl, B., and Rignot, E. (2012). Mapping of Ice Motion in Antarctica Using Synthetic-Aperture Radar Data. *Remote Sensing*, 4(12):2753–2767.

Natural Resources Canada (2014). Polarization in radar systems. http://www.nrcan.gc.ca/node/9567. Accessed 14 May 2018.

Normand, J. C. L. and Heggy, E. (2015). InSAR assessment of Surface Deformations in Urban Coastal Terrains Associated With Groundwater Dynamics. *IEEE Transactions on Geoscience and Remote Sensing*, 53(12):6356–6371.

Oost, R. (2016). A SAR-derived long-term record of glacier evolution in North-West Greenland. Master's thesis, Delft University of Technology.

QGIS Development Team (2017). QGIS (Version 2.18). http://qgis.org. Accessed 19 Feb. 2018.

Rees, D. (2011). On thin ice.

Rignot, E. (2004). Accelerated ice discharge from the Antarctic Peninsula following the collapse of Larsen B ice shelf. *Geophysical Research Letters*, 31(18).

Rignot, E. (2017). MEaSUREs InSAR-Based Antarctica Ice Velocity Map, Version 2.

Rignot, E., Jacobs, S., Mouginot, J., and Scheuchl, B. (2013). Ice-Shelf Melting Around Antarctica. *Science*, 341(6143):266–270.

Rignot, E., Mouginot, J., and Scheuchl, B. (2011a). Ice Flow of the Antarctic Ice Sheet. *Science*, 333(6048):1427–1430.

Rignot, E., Velicogna, I., van den Broeke, M. R., Monaghan, A., and Lenaerts, J. T. M. (2011b). Acceleration of the contribution of the greenland and antarctic ice sheets to sea level rise. *Geophysical Research Letters*, 38(5):n/a–n/a.

SCAR Antarctic Digital Database (2016). British Antarctic Survey Geodata Portal - Antarctic Digital Database. http://add.antarctica.ac.uk/repository. Accessed 2 Nov. 2017.

SkyGeo (n.d.). InSAR Technical Background. https://skygeo.com/insar-technical-background/. Accessed 27 Dec. 2017.

Stanford Radar Interferometry Research Group (2003). SNAPHU: Statistical-Cost, Network-Flow Algorithm for Phase Unwrapping. https://web.stanford.edu/group/radar/softwareandlinks/sw/snaphu/.

Tian, B., Li, Z., Tang, P., Zou, P., Zhang, M., and Niu, F. (2016). Use of Intensity and Coherence of X-Band SAR Data to Map Thermokarst Lakes on the Northern Tibetan Plateau. *IEEE Journal of Selected Topics in Applied Earth Observations and Remote Sensing*, 9(7):3164–3176.

Torres, R., Snoeij, P., Geudtner, D., Bibby, D., Davidson, M., Attema, E., Potin, P., Rommen, B., Floury, N., Brown, M., Traver, I. N., Deghaye, P., Duesmann, B., Rosich, B., Miranda, N., Bruno, C., L'Abbate, M., Croci, R., Pietropaolo, A., Huchler, M., and Rostan, F. (2012). GMES Sentinel-1 mission. *Remote Sensing of Environment*, 120:9–24.

TU Delft Radar Group (2017). Delft Object-oriented Radar Interferometric Software (Version 5.0). https://github.com/TUDelftGeodesy/Doris. Accessed 30 Dec. 2017.

Ulaby, F. T., Moore, R. K., and Fung, A. K. (1981). *Microwave Remote Sensing Active and Passive*. The Artech House Remote Sensing Library.

Yague-Martinez, N., Prats-Iraola, P., Rodriguez-Gonzalez, F., Brcic, R., Shau, R., Geudtner, D., Eineder, M., and Bamler, R. (2016). Interferometric Processing of Sentinel-1 TOPS Data. *IEEE Transactions on Geoscience and Remote Sensing*, 54(4):2220–2234.

Zebker, H. and Hoen, E. W. (2000). Penetration depths inferred from interferometric volume decorrelation observed over the Greenland ice sheet. *IEEE Transactions on Geoscience and Remote Sensing*, 38(6):2571–2583.

Zhou, X., Chang, N.-B., and Li, S. (2009). Applications of SAR Interferometry in Earth and Environmental Science Research. *Sensors*, 9(3):1876–1912.

# A SUPPLEMENTARY IMAGES

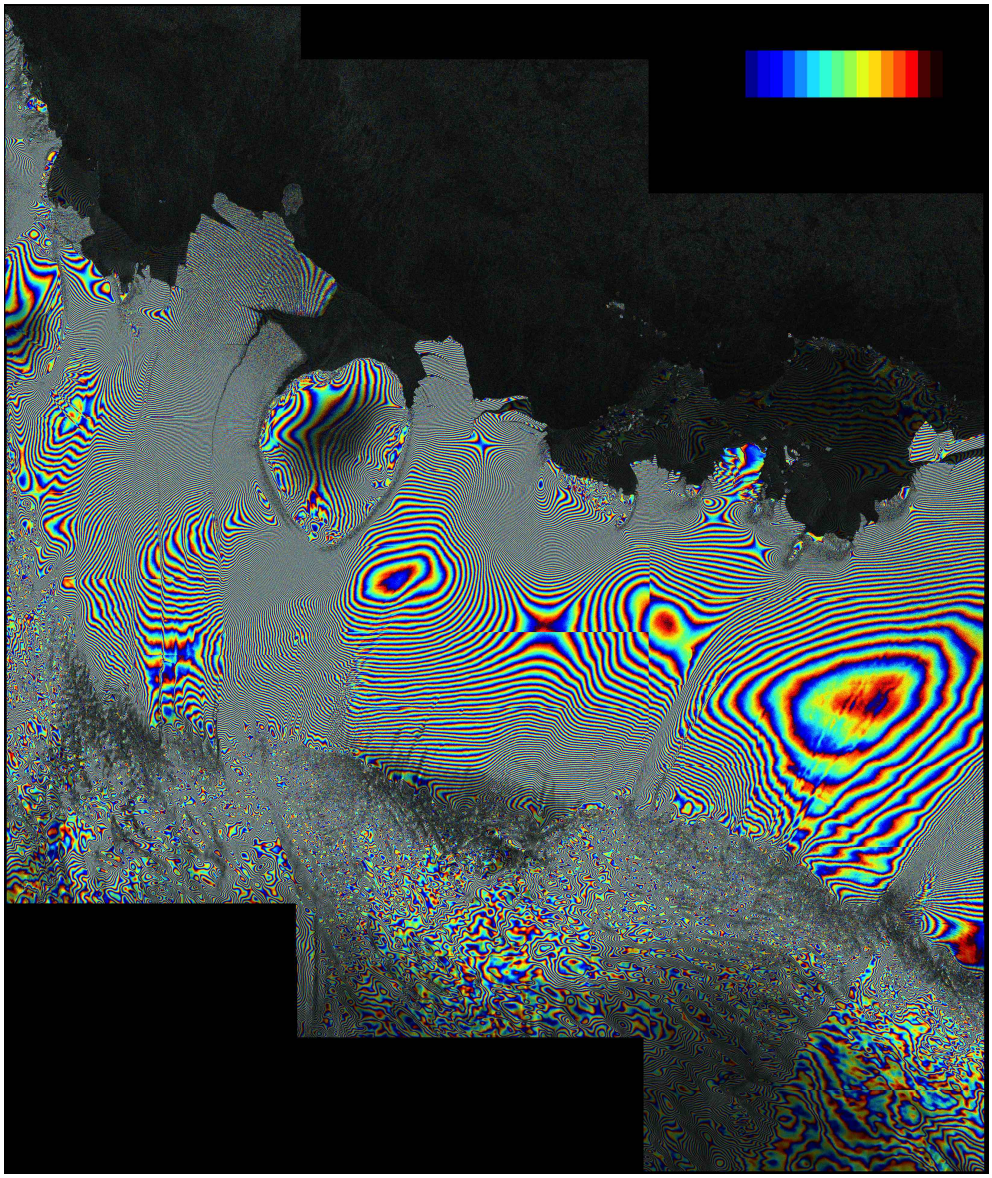

**Figure A.1:** Selection of inspected bursts

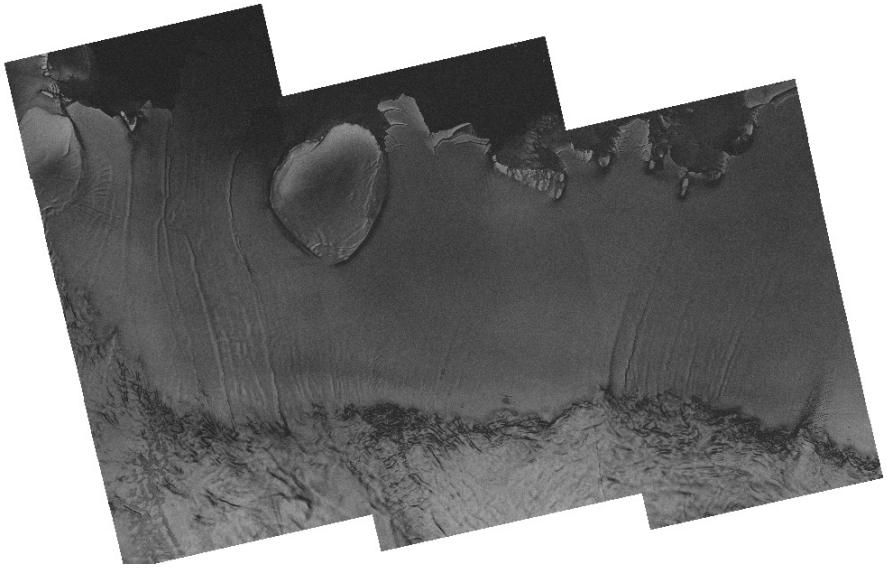

**Figure A.2:** Average coherence map

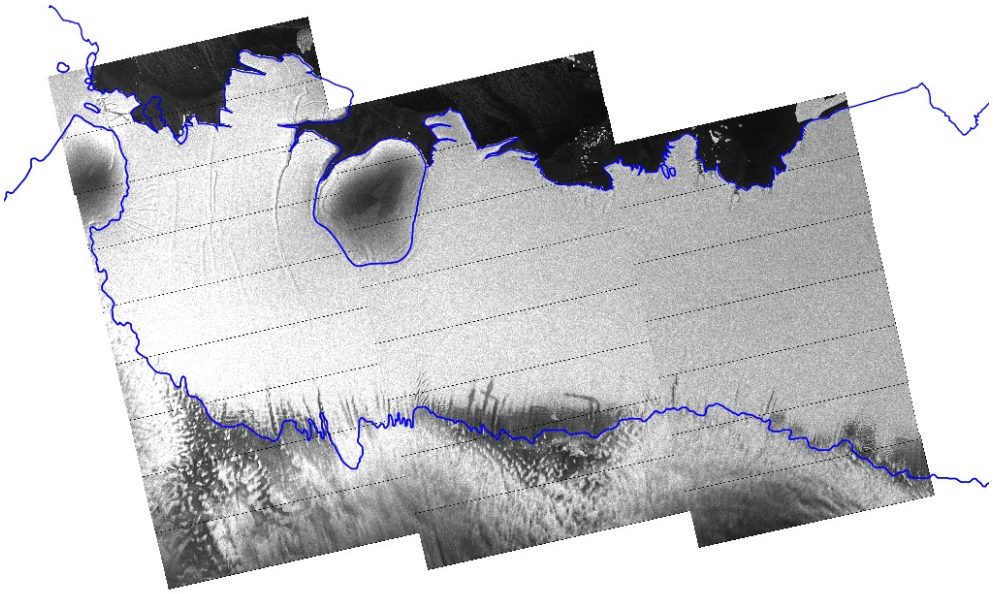

**Figure A.3:** Amplitude on 05/10/2017 fitted on map

# B | SUPPLEMENTARY CONCEPTS

## SASTRUGI

Sastrugi are the ridge-shaped features shown in Figure 4.13a. They can be formed under the influence of the local climate. In this study, they can be a disrupting feature as they have irregular patterns in amplitude and coherence, and may contribute to the forming of meltwater.

## POLARISATION

When the electromagnetic wave travels in a 3D Cartesian system, its propagation direction is defined as $z$-direction, and the oscillation is in the plane perpendicular to it, defined as $xy$-plane. The trace of the oscillation front forms the type of polarisation [Ulaby et al., 1981]. The polarisation patterns used in SAR systems are usually linear horizontal and linear vertical polarisation, referring to the oscillation along $y$-direction and $x$-direction respectively. They are then referred to as HH, HV, VH, VV, where the first letter is the transmitted polarisation and the second is the received. Depending on how many combinations are incorporated in a SAR system, the system is defined as single-polarised, dual-polarised and quad-polarised [Natural Resources Canada, 2014].

## SAR TRACKS

Ascending and descending track refer to the flight direction of the satellite. An ascending track is the direction where the satellite goes towards the north pole and a descending one is on the contrary. This concept is used for mapping. According to the ascending or descending track, the data are interpolated to a regular *geotiff* grid by using a bilinear interpolation. Figure B.1 is a depiction of the correspondence between the regular grid and the image coordinates of ascending and descending tracks respectively.

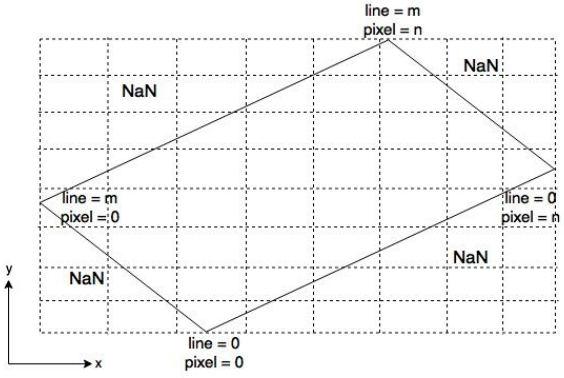


**(a)** Ascending burst

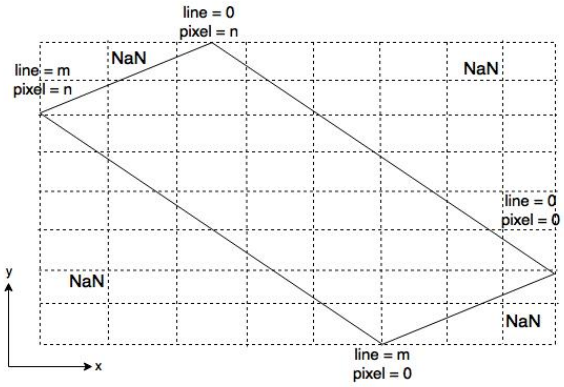


**(b)** Descending burst

**Figure B.1:** Map fitting

## DORIS PROCESSING

With the Sentinel-1 data and orbit information obtained, DORIS starts coarse-orbit coregistration. The basic function used in this step is

$$P_s(line, pixel) = P_m(line, pixel) + offset(line, pixel) \tag{B.1}$$

where $P_m$ is a point in the master image and $P_s$ is in the slave [Delft Institute of Earth Observation and Space Systems (DEOS), 2008]. The aim is to find the *offset* between the images. First, a point $P$ in the master image with the coordinate in line and pixel is projected on an ellipsoid by using the position, time and relevant properties of the satellite. Then for the slave image, the position in the *(line, pixel)* coordinate is computed corresponding to the point $P$ on the ellipsoid. Finally, the offset between master and slave images is calculated with Equation B.1 [Delft Institute of Earth Observation and Space Systems (DEOS), 2008]. The purpose of this process is to align images in the same dimensions and coordinates to facilitate further computations.

Deramping is a step to remove a linear frequency modulation in the IW data introduced by the scanning pattern of TOPSAR [Miranda, 2015]. The technical details are elaborated in Miranda [2015], and implemented internally in DORIS, hence are not introduced in this document specifically. However, what is important about this step is that the data should be deramped before being resampled, and this process should be reversed afterwards (reramp).

After deramping, the pre-defined DEM is used for coregistration again. For each DEM point, the corresponding points in the master and slave images are calculated and the offset obtained. Then, a linear interpolation of the offsets is applied to the master image grid. With the offsets computed and interpolated, the slave image is resampled with respect to the geometry of the master image [Delft Institute of Earth Observation and Space Systems (DEOS), 2008].

When an azimuth coregistration error is present, a phase jump will occur on the boundary of two adjacent bursts. This shall be estimated and corrected via an enhanced spectral diversity (ESD) approach [De Zan et al., 2014].

To generate interferograms at burst level, two types of reference phase are computed and subtracted from the data. One is the flat-earth correction, which is introduced by the coordinate reference system (CRS) surface. The other is the phase caused by

topography. Basically, with the InSAR geometry (Figure B.2), the reference phase $\phi_R$ is computed with

$$B_{\parallel} = r_1 - r_2 \tag{B.2}$$

$$\phi_R = -\frac{4\pi}{\lambda} B_{\parallel} \tag{B.3}$$

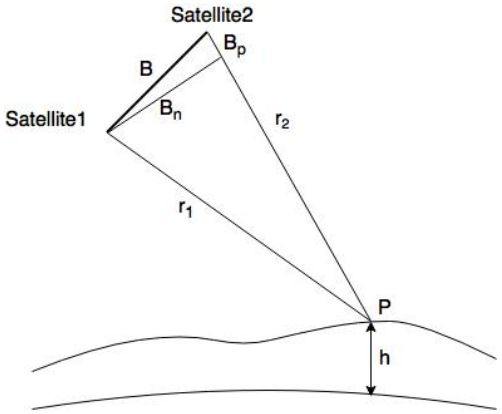


**Figure B.2:** InSAR geometry (modified from Luzi [2010])

For each point, the location is expressed in 3D Cartesian coordinates $(x, y, z)$. To georeference the point, the Bowring algorithm is used, as Algorithm B.1 shows.

**Algorithm B.1:** Bowring Algorithm

**Input:** $(x, y, z)$ coordinates and the semi-major and semi-minor axes $a$, $b$ of the ellipsoid

**Output:** $(\phi, \lambda, h)$ coordinates

1 $e^2 = \frac{a^2 - b^2}{a^2}$
2 $e'^2 = 1 - e^2 = \frac{a^2 - b^2}{b^2}$
3 $r = \sqrt{x^2 + y^2}$
4 $\nu = arctan2(z \cdot a, r \cdot b)$
5 $\phi = arctan2(z + e'^2 \cdot b \cdot sin^3\nu, r - e'^2 \cdot a \cdot cos^3\nu)$
6 $\lambda = arctan2(y, x)$
7 $N = a/\sqrt{1 - e^2 sin^2\phi}$
8 $h = r/cos\phi - N$

# C INSAR COREGISTRATION

Ideally, the coherence of the image should be as high as possible, which indicates a fine coregistration. And from the well-coregistered images, the surface and subsurface anomalies such as intensive melting, effect from the wind and water bodies can be inferred. While the main function of DORIS Sentinel-1 processing only applies the orbit, DEM and the ESD technique, cross-correlation is also a widely-used method for fine coregistration [Yague-Martinez et al., 2016]. This includes ICC and CCC, their difference being using both amplitude and phase information (CCC) and using amplitude only (ICC). According to De Zan [2014], CCC has a lower variance compared to ICC, thus yielding a higher accuracy of coregistration. But the robustness of CCC relies on the stability of the phase signal, which may fail in such a dynamic region [Oost, 2016]. Furthermore, Yague-Martinez et al. [2016] proposed that ESD may give a better azimuth accuracy than ICC. Algorithm C.1 and Algorithm C.2 contain the main steps to implement the coregistration.

**Algorithm C.1:** ICC method

**Input:** The data file $i_1$ (master), $i_2$ (slave), reference phases $\phi_{R1}$, $\phi_{R2}$ and a pre-defined block size

**Output:** The coregistered data

$\phi_{R1}, \phi_{R2} \leftarrow$ assign the correct signs with respect to the dates
$i_1 = abs(i_1)$
$i_2 = abs(i_2)$
**if** $size(i_1) = size(i_2)$ **then**
    $I_{12} = i_1 i_2^* exp(j(\phi_{R1} + \phi_{R2}))$
    $n \leftarrow$ get the number of blocks in the burst
    **for** $j \leftarrow 1$ **to** $n$ **do**
        $b_1, b_2 \leftarrow$ extract block from $i_1, i_2$
        $b_1, b_2 \leftarrow$ optimise block size for fast Fourier transform (FFT)
        $b_k = b_k - mean(b_k), k = 1, 2$
        $F = fft(b_2) \odot conj(fft(b_1))$
        $f = fftshift(ifft(F))$
        $\delta x, \delta y \leftarrow index(max(f)) - shape(f)/2$
        $\delta x, \delta y \leftarrow$ oversample to subpixel precision
    $i_{2r} \leftarrow$ resample the offsets to the whole burst

And based on the methodology in Section 3.3, swath No. 1, burst No. 3 of ascending track No. 59 is taken as the sample burst to assess the quality of interferograms generated by different methods. It is highlighted in Figure A.1. Because the CCC method requires coherence between the images [De Zan, 2011], the data from Oct. 5 to Oct. 29 are taken as an example, and the master date is Oct. 17.

The images are not georeferenced at this step, so the coordinates are shown in kilometres, originating from the first line, first pixel.

The main criterion to compare the methods is whether there is an improvement in coherence. It is an indicator of whether the images are properly coregistered. From Figure C.1 it can be seen that, ICC shows a higher coherence than the other methods

**Algorithm C.2:** CCC method

**Input:** The data file $i_1$ (master), $i_2$ (slave), and offsets per block computed from ICC

**Output:** The coregistered data

$n \leftarrow$ get the number of blocks in the burst
**for** $j \leftarrow 1$ **to** $n$ **do**
  $b_1, b_2 \leftarrow$ extract block from $i_1, i_2$
  $b_1, b_2 \leftarrow$ optimise block size for FFT
  $a, r = shape(b_1)\ k_a = fftfreq(a)$
  $k_r = fftfreq(r)$
  $b_2' = fft(b_2)exp(-2\pi j \cdot \delta x \cdot k_r)$
  $b_2' = b_2'exp(-2\pi j \cdot \delta y \cdot k_a)$
  $b_2' = ifft(b_2')$
  $I_{12} = b_2' \odot conj(b_1)$
  $fmax \leftarrow$ frequency peak of $I_{12}$
  $b_2'' \leftarrow$ deramp $b_2'$ with the frequency peak
  $F = fft(b_2'') \odot conj(fft(b_1))$
  $f = fftshift(ifft(F))$
  $\delta x, \delta y \leftarrow index(max(f)) - shape(f)/2$
  $\delta x, \delta y \leftarrow$ oversample to subpixel precision
$i_{2r} \leftarrow$ resample the offsets to the whole burst

in general, but noise can be involved during offset resampling. This may corrupt the lake features. CCC on the other hand, does not have a remarkable improvement in coherence. For the purpose of this study, the original output is used.

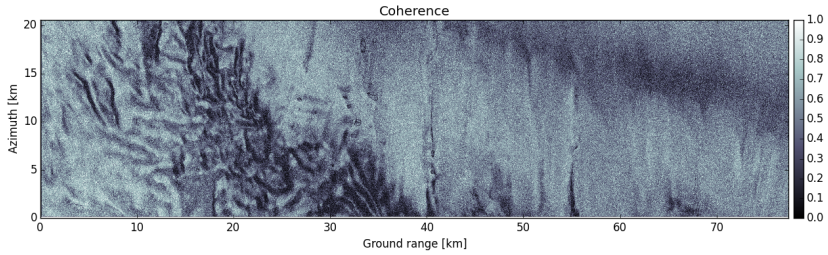


**(a)** Coherence between 29/10/2017 and 17/10/2017

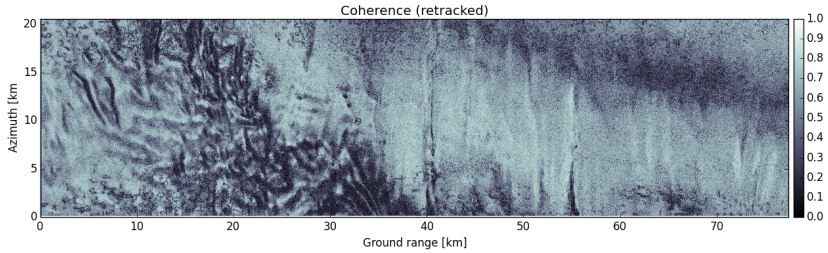


**(b)** Coherence between 29/10/2017 and 17/10/2017 from ICC

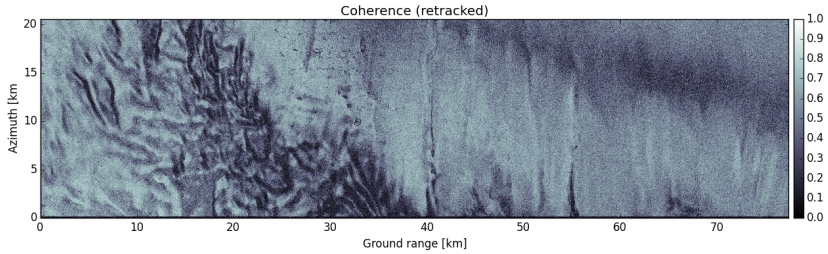


**(c)** Coherence between 29/10/2017 and 17/10/2017 from CCC

**Figure C.1:** Coherence between 29/10/2017 and 17/10/2017 from different methods

# D DETRENDING

As the interferograms provide the phases as wrapped phases, where an ambiguity within $2\pi$ exists, there is the need of unwrapping them in order to get a definitive deformation information. With respect to the local topography and ice movement, the relative movement as a result of lake filling and drainage can be referred to as a high-frequency signal. The aim of detrending is to emphasise the high frequency. This can be done by applying a high-pass filter, or fitting a plane or curvature and remove the overall trend. The results can be seen in the following figures. Because the Butterworth filter gives more details than the other methods, it is adopted by this study.

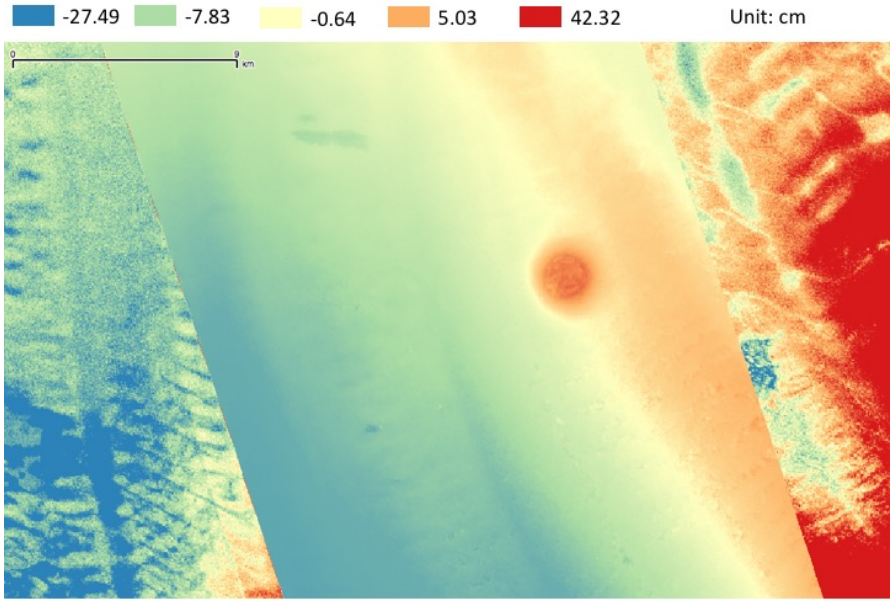


**Figure D.1**: Plane-fitting

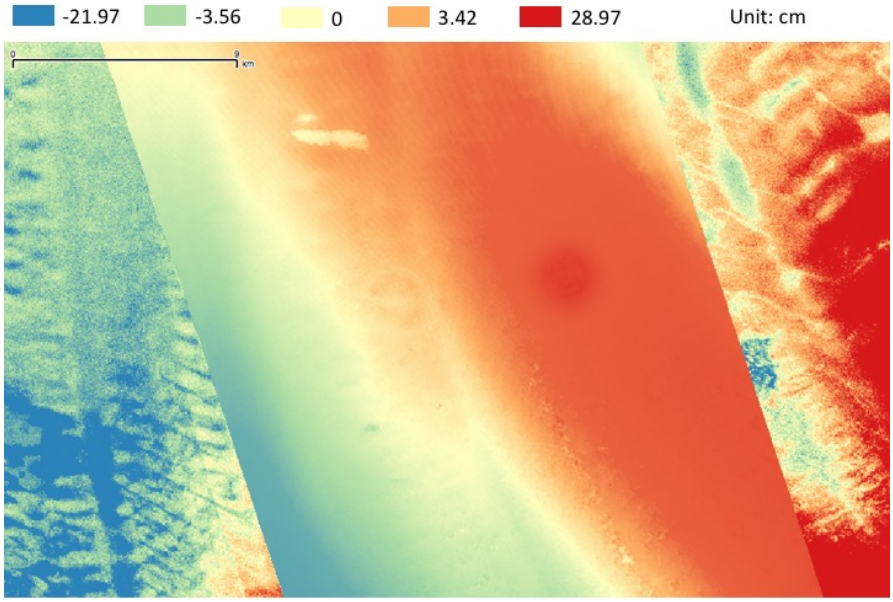


**Figure D.2:** Curvature-fitting

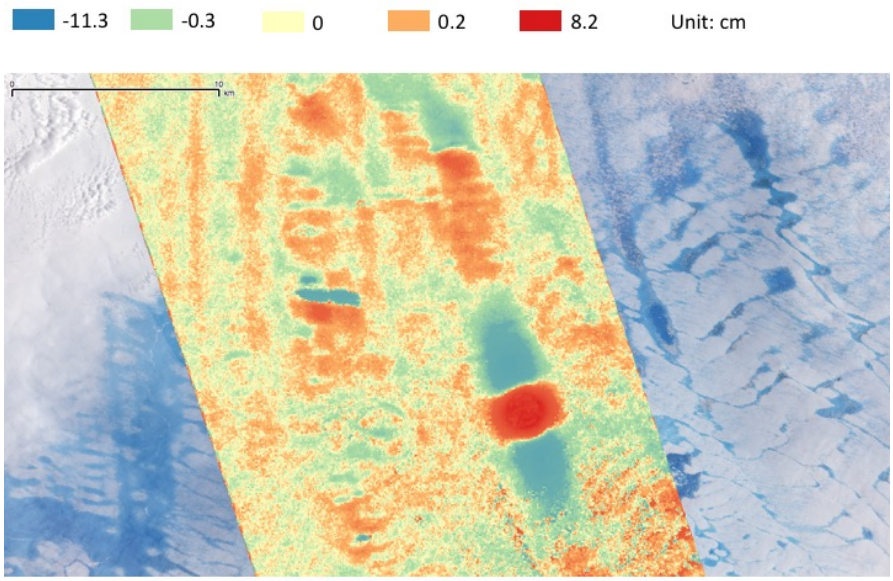


**Figure D.3:** Butterworth high-pass filter

# E REFLECTION

## THE RELATIONSHIP BETWEEN THE METHODICAL LINE OF APPROACH OF THE MASTER GEOMATICS AND THE METHOD CHOSEN BY THE STUDENT IN THIS FRAMEWORK

Because the method chosen by the student contains both aspects from the Master Geomatics and the Master Geoscience and Remote Sensing, the methodical line of approach of the Master Geomatics is rather a part of the method in this framework.

## THE RELATIONSHIP BETWEEN THE CONDUCTED RESEARCH AND APPLICATION OF THE FIELD GEOMATICS

Although this research is specifically interested in a relatively isolated and purely natural region on Earth instead of an urban area, the InSAR technique has been actively applied to measuring urban developments such as tunnels and terrain deformations. On the other hand, the observation of the natural phenomenon can be a helpful reference in spatial decision making, which is also important in the Geomatics field. From a curriculum perspective, the knowledge of mapping and open data management touched by this study has been covered by the Geomatics programme.

## THE RELATIONSHIP BETWEEN THE PROJECT AND THE WIDER SOCIAL CONTEXT

Compared to the urban environment, the ice shelf is highly dynamic, thus the study is expected to exploit the potential of InSAR applications under more dynamic circumstances. With the wider use of InSAR, more information about the natural and built environment can be acquired, therefore the public can expect to learn more about the natural environment and how human may interact with it.

## COLOPHON

This document was typeset using LaTeX. The document layout was generated using the `arsclassica` package by Lorenzo Pantieri, which is an adaption of the original `classicthesis` package from André Miede.